

DRAFT VERSION JANUARY 10, 2020

Preprint typeset using L<sup>A</sup>T<sub>E</sub>X style AASTeX6 v. 1.0

EQUILIBRIUM TIDAL RESPONSE OF JUPITER: DETECTABILITY BY *JUNO*  
SPACECRAFT

SEAN M. WAHL<sup>1</sup>

Department of Earth and Planetary Science, University of California, Berkeley, CA, 94720, USA

MARZIA PARISI<sup>2</sup>

Jet Propulsion Laboratory, California Institute of Technology, Pasadena, CA 91109, USA

WILLIAM M. FOLKNER<sup>3</sup>

Jet Propulsion Laboratory, California Institute of Technology, Pasadena, CA 91109, USA

WILLIAM B. HUBBARD<sup>4</sup>

Lunar and Planetary Laboratory, The University of Arizona, Tucson, AZ 85721, USA

BURKHARD MILITZER<sup>5</sup>

Department of Earth and Planetary Science; Department of Astronomy, University of California, Berkeley, CA,  
94720, USA

<sup>1</sup>swahl@berkeley.edu

<sup>2</sup>marzia.parisi@jpl.nasa.gov

<sup>3</sup>william.m.folkner@jpl.nasa.gov

<sup>4</sup>hubbard@lpl.arizona.edu

<sup>5</sup>militzer@berkeley.edu

## ABSTRACT

An observation of Jupiter’s tidal response is anticipated for the on-going *Juno* spacecraft mission. We combine self-consistent, numerical models of Jupiter’s equilibrium tidal response with observed Doppler shifts from the *Juno* gravity science experiment to test the sensitivity of the spacecraft to tides raised by the Galilean satellites and the Sun. The concentric Maclaurin spheroid (CMS) method finds the equilibrium shape and gravity field of a rotating, liquid planet with the tide raised by a satellite, expanded in Love numbers ( $k_{nm}$ ). We present improvements to CMS theory that eliminate an unphysical center of mass offset and study in detail the convergence behavior of the CMS approach. We demonstrate that the dependence of  $k_{nm}$  with orbital distance is important when considering the combined tidal response for Jupiter. Conversely, the details of the interior structure have a negligible influence on  $k_{nm}$ , for models that match the zonal harmonics  $J_2$ ,  $J_4$  and  $J_6$ , already measured to high precision by *Juno*. As the mission continues, improved coverage of Jupiter’s gravity field at different phases of Io’s orbit is expected to yield an observed value for the degree-2 Love number ( $k_{22}$ ) and potentially select higher-degree  $k_{nm}$ . We present a test of the sensitivity of the *Juno* Doppler signal to the calculated  $k_{nm}$ , which suggests the detectability of  $k_{33}$ ,  $k_{42}$  and  $k_{31}$ , in addition to  $k_{22}$ . A mismatch of a robust *Juno* observation with the remarkably small range in calculated Io equilibrium  $k_{22} = 0.58976 \pm 0.0001$ , would indicate a heretofore uncharacterized dynamic contribution to the tides.

*Keywords:* Jovian planets, Tides, Interiors, Jupiter

## 1. INTRODUCTION

Since orbital insertion in July of 2016, the *Juno* spacecraft has yielded robust measurements of even (Folkner et al. 2017) and odd (Iess et al. 2018) zonal harmonics of Jupiter’s gravitational field. These high-precision gravity measurements inform our understanding of Jupiter’s interior structure (Wahl et al. 2017b; Nettelmann 2017; Debras & Chabrier 2019) and wind structure (Kaspi et al. 2017a, 2018; Guillot et al. 2018). As the spacecraft makes additional orbits, it is expected to constrain the tidal response of the planet in terms of the second degree Love number,  $k_{22}$ , and possibly higher degree  $k_{nm}$  as well. Prior knowledge of the higher degree  $k_{nm}$  from theoretical models also aids in the fitting of a gravity solution to the *Juno* Doppler radio measurements.

The concentric Maclaurin spheroid (CMS) method (Hubbard 2012, 2013) is a non-perturbative, numerical method for calculating the self-consistent mass distribution and gravity field of a rotating liquid body. In two-dimensions, the CMS approach allows efficient and precise exploration of interior structure models (Militzer et al. 2019). In three-dimensions, the CMS method permits a precise calculation of equilibrium tidal response, yielding both  $k_{22}$  and higher degree  $k_{nm}$  (Wahl et al. 2017a, 2016). The CMS calculations demonstrated a significant effect from the rotational flattening of Jupiter and Saturn, manifesting in an enhanced  $k_{22}$  compared with calculations treating the tidal response as a perturbation from a sphere (Gavrilov & Zharkov 1977), as well as splitting of the higher degree  $k_{nm}$ . In this paper we present improvements to the CMS equilibrium tidal response calculations, including a solution to the unphysical center of mass offsets described in Wahl et al. (2017a). We also study in greater detail the convergence behavior of CMS tidal response calculations, and how this affects the precision to which we can determine different values of  $k_{nm}$  for the four

Galilean satellites, and the Sun.

A preliminary value of  $k_{22} = 0.625 \pm 0.06$  was presented in the *Juno* gravity solution of [Iess et al. \(2018\)](#), consistent with the enhanced value predicted from CMS, but not sufficiently precise to fully characterize the nature of the tidal response. In the case of Saturn, astrometric observations ([Lainey et al. 2017](#)) yield a  $k_{22}$  that is below the value for a equilibrium tide to their reported uncertainty, but still enhanced compared to the prediction from perturbation theory applied to a spherical Saturn.

A major outstanding question is whether Jupiter’s tidal response can be adequately described by equilibrium theory alone, as addressed in this paper, or whether there is a detectable dynamic contribution to the tides. The equilibrium tidal response treated here assumes that the rotating liquid interior responds instantaneously to the perturbing satellite<sup>1</sup>. In the co-rotating frame of the planet, we find the equilibrium tidal distortion, fully determined by the orbit and  $k_{nm}$  calculated for each perturbing satellite. In contrast, dynamic tides are a frequency dependent response, affected by proximity to resonances and excitation and waves as the tidal perturbations interact with interior structural features, such as stable layers or density discontinuities ([Marley & Porco 1993](#); [Fuller 2014b,a](#)). Calculations of dynamic tides rely on normal mode calculations ([Durante et al. 2017](#)), related to techniques used in astroseismology [Chaplin & Miglio \(2013\)](#). While special cases of dynamic tidal response been demonstrated to result in a small enhancement to  $k_{22}$  ([Gavrilov & Zharkov 1977](#)), a comprehensive treatment of dynamic tidal response of a Jovian planet with rotational flattening has not been attempted. However, once an interior model is fitted to observed zonal harmonic coefficients,  $J_n$ , its equilibrium tidal response coefficients,  $k_{nm}$ , are determined with little remaining uncertainty. Thus, measurements of  $k_{nm}$  that disagree with the equilibrium response are evidence of a dynamic tidal response.

<sup>1</sup> The terms “equilibrium tides” and “static” tides have been used interchangeably to refer to the same phenomenon in the literature. We elect to use “equilibrium” in this paper

In [Wahl et al. \(2016\)](#), we presented preliminary calculations of Jupiter’s equilibrium tidal response for a range of different interior models ([Hubbard & Militzer 2016](#)) based on pre-*Juno* knowledge and assumptions about the planet’s interior. This included a wide range of models, in part because of a disagreement of the JUP310 gravity solution ([Jacobson 2013](#)) with earlier gravity solutions ([Campbell & Synnott 1985](#); [Jacobson 2003](#)). The pre-*Juno* gravity solution permitted two or three-layer interior structure models with a variety of hydrogen-helium equations of state ([Saumon & Guillot 2004](#); [Militzer et al. 2008](#); [Nettelmann et al. 2012](#); [Miguel et al. 2016](#); [Hubbard & Militzer 2016](#)). As of the *Juno* gravity solution presented by [Iess et al. \(2018\)](#), there are now precise determinations of the even gravity harmonics up to  $J_{10}$  and odd harmonics up to  $J_9$ . The low-order, even gravity harmonics  $J_2$ ,  $J_4$  and  $J_6$ , are all determined to  $\sim 10^{-8}$  or better. When taken into consideration with state of the art equations of state for hydrogen-helium mixtures ([Vorberger et al. 2007](#); [Militzer 2013](#)) and constraints on atmospheric composition and temperature, these low-order harmonics place strong constraints on the viable interior structure models ([Wahl et al. 2017a](#); [Nettelmann 2017](#); [Debras & Chabrier 2019](#); [Militzer et al. 2020](#)), suggesting that Jupiter’s interior structure is more complicated than previously thought. [Nettelmann \(2019\)](#) presented calculations of equilibrium  $k_{nm}$  of an interior structural fit to earlier *Juno* gravity solution ([Folkner et al. 2017](#)). In this paper we present results for the equilibrium tidal response of Jupiter, with the constraints from the most recent *Juno* gravity solution ([Iess et al. 2018](#)) and an improved implementation of the CMS method. We consider the ranges in tidal response expected from uncertainty from the interior structure, deep winds and measurements of the relevant physical parameters, as well as the numerical precision of CMS method. Characterizing this uncertainty in modeling the equilibrium tide is necessary to know whether a precise measurement of  $k_{nm}$  alone is sufficient to detect a dynamic contribution, and distinguish it from the equilibrium contributions.

In Section [2.1](#) we present an overview of the CMS method focused on the details pertinent to the

calculation of the equilibrium tidal response. In Section 2.2 we describe the improvements to the CMS approach for equilibrium tidal calculations, and their effect on the calculations. In 2.3 we describe interior models used in this study, as well as our methods for quantifying the possible range of  $k_{nm}$  from interior structure and winds. In Section 3.1 we look at the convergence of the CMS models with various parameters to quantify precision to which different  $k_{nm}$  can be predicted. In Section 3.2 we present, in detail, the tidal response of Jupiter to the four Galilean satellites and the Sun, and consider *Juno*'s ability to sample that tidal response. Finally in Section 3.4, we test the sensitivity of the *Juno* Doppler gravity measurements to the calculated  $k_{nm}$ , and discuss the significance of the higher degree  $k_{nm}$  to the fitting of a gravity solution by the *Juno* gravity science experiment.

## 2. METHODS

### 2.1. CMS method

The *concentric Maclaurin spheroid* method (CMS) is a non-perturbative, iterative method to find the gravity field of a liquid body, which was formulated by Hubbard (2012, 2013) and extended to three dimensions by Wahl et al. (2017a).

In this method, a continuous density structure is discretized into  $N$  nested, constant-density spheroids, as shown in Fig. 1. The planet's self-gravity,  $V$ , is calculated as a volume-integrated function of all spheroids in their current configuration, and combined with a centrifugal potential,  $Q$ , and an external potential from a perturbing satellite,  $W$ , into a single effective potential,

$$U(\mathbf{r}) = V(\mathbf{r}) + Q(\mathbf{r}) + W(\mathbf{r}) \quad (1)$$

The shape of each spheroid is then adjusted until the surface of each becomes an equipotential surface of  $U$ .

Given a prescribed interior density structure, the non-spherical contributions to the potential are parameterized by three non-dimensional numbers. First is the relative strength of the centrifugal

potential,

$$q_{\text{rot}} = \frac{\omega^2 r_J^3}{GM_J}, \quad (2)$$

where  $\omega$  is the sidereal rotation frequency,  $r_J$  is the equatorial radius of the Jupiter,  $G$  is the universal gravitational constant and  $M_J$  is the mass of Jupiter. The second describes the relative strength of the tidal perturbation,

$$q_{\text{tid}} = -\frac{3m_s r_J^3}{M_J R^3}, \quad (3)$$

where  $m_s$  is the mass of the perturbing satellite (or the Sun) and  $R$  is the orbital distance. Last is the ratio of the satellite's orbital distance to the planet's radius,

$$R/r_J. \quad (4)$$

The relevant physical parameters for Jupiter, its satellites and the Sun are summarized in Tab. 1. The uncertainty of  $q_{\text{rot}}$  is dominated by the  $\sim 4$  km uncertainty in  $r_J$ . It is worth noting that although a CMS calculation is performed for a single set of parameters,  $q_{\text{tid}}$  and  $R/r_J$  vary with time due to the eccentricity of the orbit, which must be taken into account when translating the calculated  $k_{nm}$  into a gravity signal.

The zonal,  $J_n$ , and tesseral,  $C_{nm}$  and  $S_{nm}$ , harmonics of the gravity field (depicted in Fig. 2) can be calculated by integrating over the density and shape of a converged CMS model (Wahl et al. 2017a). For Jupiter and its Galilean satellites  $q_{\text{tid}} \ll q_{\text{rot}}$ , which means that the equilibrium tidal response from each satellite can be calculated independently, and the resulting  $C_{nm}$  and  $S_{nm}$  can be linearly superimposed to obtain the total equilibrium tidal response. The calculations can be further simplified by assuming that the satellites reside in the planet's equatorial plane since the Galilean moons each exhibit a small orbital inclination. Under these assumptions, we perform CMS calculations for a single satellite at a time, with a fixed position in the equatorial plane.

As per convention (Zharkov & Trubitsyn 1978), the tidal Love numbers represent ratio of the tidally

induced gravity moments to the strength of perturbing tidal potential, which can be represented as

$$k_{nm} = -\frac{3(n+m)!(C_{nm} - C_{nm}^0)}{2(n-m)!P_n^m(0)q_{\text{tid}}}\left(\frac{r_{\text{eq}}}{R}\right)^{2-n}, \quad (5)$$

where  $m \leq n$  and  $P_n^m$  are the associated Legendre polynomials<sup>2</sup>. Here  $C_{nm}^0$  is the harmonic for the unperturbed body (i.e. with rotation, but without tides). For  $m \neq 0$ ,  $C_{nm}^0 = 0$ , but with rotation

$$C_{n0}^0 = -2J_n^0, \quad (6)$$

where  $J_n$  are the corresponding zonal harmonics from an axisymmetric calculation with the same  $q_{\text{rot}}$ .

For this reason the  $k_{n0}$  cannot be directly measured in the *Juno* Doppler data, as their contribution is indistinguishable from contributions from rotation and interior density distribution. The eccentricity of the satellite orbit induces a small, time-variable component of  $C_{n0}$ , that might be detectable as a variation of the observed  $J_n$  with the satellites orbital phase. If the tidal perturbers are located on the equatorial plane, as we assume, then all  $k_{nm}$  with odd values of  $n-m$  are zero. For a non-rotating planet, the  $k_{nm}$  with the same degree  $n$  are degenerate with order  $m$ . Jupiter, on the other hand, exhibits significant splitting of these  $k_{nm}$  due to the significant rotational flattening.

## 2.2. Tidal Response Calculations

In this section, we provide details to perform accurate tidal response calculation with the CMS method and discuss a number of assumptions and approximations. Most importantly, we only deal with the *equilibrium* response and assume the planet responds instantaneously to an external perturbation by a satellite. Since the satellite's diameter is small compared to its orbital distance,  $\mathbf{R}$ , it is well-justified to treat the satellite as a point mass,  $m_s$ . Its gravitational potential is given by

$$W(\mathbf{r}, \mathbf{R}) = \frac{Gm_s}{|\mathbf{R} - \mathbf{r}|}, \quad (7)$$

<sup>2</sup> This equation appeared in [Wahl et al. \(2017a\)](#) with a typographical error in the prefactor



and can be expressed in terms of Legendre polynomials,

$$W(r, \mu, \phi) = \frac{Gm_s}{R} \sum_{n=0}^{\infty} \left(\frac{r}{R}\right)^n \left[ P_n(\mu)P_n(\mu_s) + 2 \sum_{m=1}^n \frac{(n-m)!}{(n+m)!} \cos(m\phi - m\phi_s) P_n^m(\mu)P_n^m(\mu_s) \right]. \quad (8)$$

where we have specified the satellites location with  $R$ ,  $\mu_s$ , and  $\phi_s$ .

For potential theory to be applicable, the tidal perturbation needs to be time independent, which means one can only derive the tidal response for an analogue system where the satellite's orbital period is set equal to the rotation period of the planet. In the rotating frame, the satellite's gravity field then becomes time independent and it is a well-posed but simplified task to determine the planet's response. There are situations where these assumptions are well justified, e.g., tidally locked exoplanets that have equal orbital and rotation periods. However, satellites in the solar system all have orbital periods that are much longer than the rotation periods of the host planets. This introduces a time dependence into the tidal perturbation and may lead to *dynamic* tidal effects. The dynamic response is typically studied by expanding the planet's response in terms of normal modes [Gavrilov & Zharkov \(1977\)](#). Even when such dynamic tidal calculations are performed for Jupiter, one expects to find a negligible tidal lag because the viscosity in giant planets is very small. A counter example are the tides on Earth, where there is a more substantial response lag for the solid mantle and crust.

The standard approach to derive a time independent solution is to remove the average force that the tidal perturber exerts on the planet ([Murray & Dermott 1999](#)). Removing the average force can be motivated by representing the planet by a system of  $N$  fluid parcels of mass  $m_i$  at locations  $\mathbf{r}_i$ . Its total energy is assumed to be given by  $\mathcal{V}(\mathbf{r}_1 \dots \mathbf{r}_N)$  and an equilibrium configuration must satisfy  $\mathbf{F}_i = \partial\mathcal{V}/\partial\mathbf{r}_i = 0$ . In order to establish the orbital distance for a given planet, we constrain the planet's center of mass to reside at  $\mathbf{R}_{\text{CM}}$ . To solve this constrained optimization problem, we

introduce the modified function,

$$\tilde{\mathcal{V}}(\mathbf{r}_1 \dots \mathbf{r}_N) = \mathcal{V}(\mathbf{r}_1 \dots \mathbf{r}_N) - \lambda \left[ \sum_i m_i \mathbf{r}_i - M \mathbf{R}_{\text{CM}} \right] , \quad (9)$$

where  $\lambda$  is a Lagrange multiplier and  $M$  is the total mass. Solving  $\partial \tilde{\mathcal{V}} / \partial \mathbf{r}_i = 0$  yields that  $\lambda$  must be equal to the average force,  $\langle \mathbf{F} \rangle$ . The equilibrium solution of the constrained system must then satisfy,  $0 = \partial \mathcal{V} / \partial \mathbf{r}_i - \langle \mathbf{F} \rangle m_i$ , which explains why one would want to remove the average force.

In the CMS calculations, we derive this average force as follows,

$$\langle \mathbf{F} \rangle = \frac{1}{M} \int d\mathbf{r} \rho(\mathbf{r}) \nabla_{\mathbf{r}} W(\mathbf{r}, \mathbf{R}) = -\frac{1}{M} \nabla_{\mathbf{R}} \int d\mathbf{r} \rho(\mathbf{r}) W(\mathbf{r}, \mathbf{R}) = -\frac{m_s}{M} \nabla_{\mathbf{R}} V(\mathbf{r} = \mathbf{R}) , \quad (10)$$

where we have integrated over all fluid parcels in the planet in the first two terms. In the last term, we have used the symmetry of the gravitational potential, which implies that the average force that the satellite exerts on the planet is equal but opposite to the force that the planet exerts on the satellite. The evaluation of the last term is straightforward within the CMS method, because the gradient is already needed to converge the spheroid shapes onto equipotential surfaces using Newton's method.

With the average force, we define a modified tidal potential

$$\tilde{W}(\mathbf{r}, \mathbf{R}) = W(\mathbf{r}, \mathbf{R}) - \langle \mathbf{F} \rangle \cdot \mathbf{r} \quad (11)$$

and introduce it into Eq. 1 before using the modified potential to construct equipotential surfaces. With this approach, one obtains a stable numerical algorithm that converges to a self-consistent CMS solution. This algorithm is used for all the results reported in this article.

With other, more approximate approaches, it is more difficult to reach well converged simulations. [Zharkov & Trubitsyn \(1978\)](#) did not derive the average force explicitly but instead removed the  $n = 1$  term from Eq. 8, which is linear in  $r$ . For point masses, this is equivalent to Eq. 10 but for an extended planet this introduces a small spurious force that lets the planet drift towards the satellite because the gravitational force is nonlinear. In the previous implementation of the CMS tidal

response calculation (Wahl et al. 2017a) that was based on Eq. 8, we noticed a small but persistent center of mass shift ( $C_{11} > 0$ ) following each iterative update of the spheroid surfaces ( $\zeta_i$ ). This was accounted for by applying a translation to all grid points after each iteration to eliminate  $C_{11}$ , but this prevented full convergence of the spheroids to equipotential surfaces with the expected numerical precision. With our new approach based on Eqs. 10 and 11, this problem has been eliminated and we now obtained well-converged equipotentials and the computed  $C_{11}$  is zero to within numerical precision.

We initialize our tidal calculations with spheroid shapes defined by the fractional radius,  $\zeta_i(\mu, \phi)$ , that we obtain from a fully converged 2D axisymmetric CMS solution,  $\zeta_i(\mu)$ . The spheroid shapes have converged when  $U(\zeta_i(\mu, \phi))$  is the same for all points in any given spheroids. We can no longer fix  $\zeta_i(\mu = 0) = 1$  since we expect two tidal bulges to form. Instead we require the volume of each spheroid to be the same as determined by the initial axisymmetric calculation. Since there is much flexibility in the 3D CMS calculation, the implementation of the volume constraint requires some care. For a given spheroid, we first compute a target potential value,  $U_i^T$  by averaging  $U(\zeta_i(\mu_k, \phi_k))$  over all spheroid points,  $k$ . We then compute vector of proposed  $\zeta$  corrections with Newton's method,

$$\Delta\zeta_i^{(k)} \equiv \Delta\zeta_i(\mu_k, \phi_k) = \frac{U(\zeta_i(\mu_k, \phi_k)) - U_i^T}{U'(\zeta_i(\mu_k, \phi_k))} \quad (12)$$

where  $U'$  is the derivative of the  $U$  with respect to  $\zeta$ . We require that all  $\Delta\zeta_i^{(k)}$  combined do not change the spheroid volume,  $\Omega_i$ . We thus remove the volume-changing vector component with

$$\vec{y}^{\text{corr}} = \vec{y} - \frac{\vec{y} \cdot \vec{x}}{\vec{x} \cdot \vec{x}} \vec{x}, \quad (13)$$

where  $\vec{y}$  and  $\vec{x}$  represent the vectors  $\Delta\zeta_i^{(k)}$  and  $d\Omega_i/d\zeta_i^{(k)}$  respectively. We then apply the corrected  $\vec{y}^{\text{corr}} \equiv \Delta\zeta_i^{(k)}$  and rescale the spheroid again to exactly match the original  $\Omega_i$ .

Once all spheroids have been updated, we compute the new  $C_{11}$  term and apply a single coherent

shift to all spheroids, so that planet’s total center of mass is again at the origin. This requires performing a spline interpolation for each spheroid over  $\mu$  and  $\phi$ , so that the pre and post-shift grid points remain on the quadrature points. In contrast to the behavior described in [Wahl et al. \(2017a\)](#), this center of mass shift gradually decreases to zero as the spheroids converge towards equipotential surfaces.

When we examine the converged CMS solutions, we notice that the centers of mass of individual outer spheroids exhibit a small shift towards the perturbing satellite, while the inner spheroids have drifted away from it, as shown in the lower panel of [Fig. 1](#). When we instead restricted the center of mass of every individual spheroids during the CMS iterations, we were not able to construct equipotential surfaces. We thus conclude that the small spheroid shifts are necessary to correctly represent how a fluid planet with a realistic interior density structure responds to the tidal perturbations.

In [Fig. 3](#) we show the spheroid shifts quantitatively for a representative CMS calculation. Over the course of the calculations the spheroids arrange themselves so that the centers of mass follow a smooth function of radius. When shown as a function of integrated mass, it can be seen that roughly half of the mass is shifted towards the satellite and the other half away, such that the planet’s total center of mass remains at the origin. The inner spheroids exhibit a larger magnitude of shift than the outer spheroids, but they also contain less mass. Depending on the magnitude of the tidal perturbation, we find the outermost spheroid to shift between  $10^{-12}$  and  $10^{-5}$  Jupiter radii.

### 2.3. Interior models

We start from the assumption of a liquid planet in hydrostatic equilibrium,

$$\nabla P = \rho \nabla U, \tag{14}$$

where  $P$  is the pressure,  $\rho$  is the mass density and  $U$  the total effective potential. The material properties of hydrogen–helium mixture, with a mass fraction of heavier elements in solution, determines a barotrope  $P(\rho)$  for the planet’s interior.

Presently, the most trusted equations of states are constructed from *ab initio* simulations using density functional molecular dynamics (DFT-MD) (Vorberger et al. 2007; Militzer 2013; Becker et al. 2015; Chabrier et al. 2019). Our models use barotropes constructed from a grid of adiabats determined by the Militzer (2013) equation of state for a hydrogen-helium mixture. The DFT-MD simulations were performed, with cells containing  $N_{He} = 18$  helium and  $N_H = 220$  hydrogen atoms, using the Perdew-Burke-Ernzerhof (PBE) functional (Perdew et al. 1996) in combination with a thermodynamic integration technique.

There was initial disagreement between different DFT-MD based equations of state for hydrogen helium mixtures, with the REOS (Nettelmann et al. 2008; Becker et al. 2015) equation of state predicting hotter, less dense barotropes (Militzer 2009; Guillot et al. 2018) than that of Militzer (2013), due to their different method for calculating the specific entropy. There is now better agreement between the independently constructed DFT equations of state (Militzer & Hubbard 2013; Schöttler & Redmer 2018; Chabrier et al. 2019), all predicting colder, denser barotropes consistent with those based on thermodynamic integration.

We follow the same treatment of specific entropy, helium and heavy-element fraction as in previous work (Hubbard & Militzer 2016; Militzer et al. 2016; Wahl et al. 2016, 2017b). The entropy,  $S$ , is a proxy for a particular adiabatic temperature  $T(P)$  relationship for a fixed composition H-He mixture ( $Y_0 = 0.245$ ). This initial composition also provides the reference barotrope densities, in which deviations from the baseline composition ( $Y_0 = 0.245$ ,  $Z_0 = 0$ ), are treated as perturbations using the additive volume law (Wahl et al. 2017a).

When the inherent density of the hydrogen–helium mixture is set by the DFT equation of state,

it is not possible to find simple 3-layer interior models that simultaneously match the *Juno* gravity solution, while satisfying atmospheric constraints on temperature and composition from the *Galileo* entry probe (Seiff et al. 1998; von Zahn et al. 1998). Satisfying all such constraints requires either more complex interior thermal and compositional structure (Debras & Chabrier 2019), contributions from deep winds (Guillot et al. 2018; Kaspi et al. 2018) or both (Militzer et al. 2020). The requisite deep wind profile decays with depth, due to interaction of the conductive fluid with the magnetic field (Cao & Stevenson 2017), and cannot be described self-consistently using a potential based theory like CMS (Militzer et al. 2019).

The Love numbers are known to be strongly correlated with  $J_n$  (Wahl et al. 2017a). We thus elect to first examine a set of simple interior models, capable of matching the updated low-order axisymmetric *Juno* gravity solution (Iess et al. 2018) with loosened compositional constraints (A1–4 in Tab. 2). We next consider the effect of deep wind profiles optimized to match the odd zonal harmonics (Kaspi et al. 2018) (B1–2 in Tab. 2). Finally, we include models in which a more complicated interior structure and deep wind profile are optimized simultaneously (Militzer et al. 2020) (C1–4 in Tab. 2). The models considering deep winds are described in more detail in Section 2.4.

The first set of models considered are 3 or 4-layer interior models modified from those presented in Wahl et al. (2017b), with parameters tuned to match  $J_2$ ,  $J_4$  and  $J_6$ . These models are denoted as A1–4 in Tab. 2, with the model  $J_n$  compared to the target values from *Juno*. The target  $J_n$  are obtained from the Iess et al. (2018) gravity solution to the *Juno* Doppler measurements Iess et al. (2018) solution. However, in this solution the reported  $J_n$  would include any tidal contribution ( $C_{n0}$ ). Thus for consistency, we subtract the calculated Io  $C_{n0}$  from the observed  $J_n$  to obtain the target  $J_n$ . For instance, the target  $J_2 = 14696.51 \times 10^{-6}$  is used instead of the observed  $J_2 = 14696.57 \times 10^{-6}$ . The interior models consist of an outer, molecular envelope, and an inner, metallic envelope separated by a transition in which helium is proposed to phase separate and rain out (Stevenson & Salpeter 1977;

Morales et al. 2013; Militzer et al. 2016). Each model includes an innermost spheroid representing a constant density central core with a fractional radius  $r/r_j = 0.15$ . The outer and inner envelope are parameterized by a set of parameters  $(S_1, Y_1, Z_1)$  and  $(S_2, Y_2, Z_2)$  respectively. The helium rain region is treated as a smooth transition of each parameter between two pressures, while the central core is treated separate from envelope parameters with its density required to conserve the total mass of the planet. A subset of these models (A3–4) also consider a dilute core with a constant enrichment of heavy elements ( $Z_3$ ) with a higher concentration than in the metallic envelope ( $Z_2$ ). Since there is a density tradeoff between parameters and a lack of constraints in the deep interior, we assume  $S_3 = S_2$  and  $Y_3 = Y_2$  for simplicity.

In model A1  $J_2$  and  $J_4$  are matched by iteratively tuning  $S_1 = S_2$  and  $Z_2$ , and  $J_6$  by tuning the pressure of helium rain onset. In other models, the pressure of helium rain onset is set to  $P = 95.4$  GPa, consistent with the Morales et al. (2013) phase curve and an outer envelope adiabat with  $S = 7.07 k_B/\text{electron}$  based on Galileo entry probe temperature measurements (Seiff et al. 1998).<sup>3</sup> In Model A2,  $J_2$  and  $J_4$  are matched to the same procedure, while  $J_6$  is matched by tuning the jump in  $\Delta S = S_2 - S_1$  across the helium rain layer. Finally, models A3 and A4 fit  $J_6$  by tuning the heavy element fraction of a dilute core,  $Z_3$ , with a fractional radius of  $r/r_j = 0.7$  and  $0.5$  respectively. Models A3 and A4 require dilute cores with  $Z_3 = 0.12$  and  $0.30$ , respectively, compared to the heavy element fraction for the deep envelope with  $Z_2 = 0.066$  in A1.

As noted previously (Wahl et al. 2017b; Guillot et al. 2018), such simple 3 or 4-layer models require outer envelopes hotter than expected based on the *Galileo* entry probe measurements (Seiff et al. 1998), when using the Militzer (2013) equation of state. These models are thus interpreted to give a rough, conservative estimate of the range of tidal responses that might be expected from variability

<sup>3</sup> This pressure is not consistent with the envelope entropy for the 3 or 4 models presented here, but we treat  $P = 95.4$  GPa as a baseline, given multiple sources of uncertainty for the onset of helium rain.

in an interior density structure alone matching the low order zonal harmonics, rather than seeking a single model to match all desired constraints.

#### 2.4. *Influence of deep winds*

The observed zonal harmonics are not due solely to a barotropic interior profile, but will have contributions from deep winds [Kaspi \(2013\)](#); [Kaspi et al. \(2017b\)](#). Due to the limitations of potential theory, differential rotation can only be implemented fully consistently for cylinders extending through the deep interior of the planet ([Wisdom & Hubbard 2016](#)). It is therefore, not possible to implement the more complex 3D wind profile expected for Jupiter, in which the cylindrical flow velocities decay rapidly at depths where conductivity becomes high enough for flows to couple to the planet’s magnetic field ([Cao & Stevenson 2017](#)). We therefore, cannot self-consistently test their effect on the tidal response ([Militzer et al. 2019](#)). As a conservative estimate, we consider interior models that fit to  $J_2$ - $J_6$  with the contributions from various wind models omitted. The first class of wind models use the  $\Delta J_n$  from [Kaspi et al. \(2018\)](#), which used the thermal wind equation to optimize a decay function for the observed surface wind profiles to match the odd zonal harmonics. The second class of wind models represent a class of models that can be found when the interior structure and wind profiles are optimized simultaneously ([Militzer et al. 2020](#)).

The second set of models in [Tab. 2](#) are constructed identically to the reference model (A1) but with the target  $J_n$  chosen to be  $J_{n,\text{Juno}} - \Delta J_n$ , where  $\Delta J_n$  is set to the contribution from the optimized deep wind profiles of [Kaspi et al. \(2018\)](#), for the longitude-independent (model B1) and longitude independent (model B2) profiles. The wind profiles that lead to these  $\Delta J_n$  are incompatible with a potential theory based method like CMS. In lieu of a consistent method for predicting the wind contribution to the tidal response, we consider the case where the winds have no direct contribution to  $k_{nm}$  and only affect the model through modifying the target  $J_n$  in the CMS calculation, to be



different from the reference model, A1. Since the true contribution to the winds to  $k_{nm}$  should partially offset this difference, this treatment should lead to conservative estimate of the range values that might result from models with winds. In Section 3.2, we demonstrate that this range is indeed small compared to Juno’s sensitivity.

Finally, we calculate the tidal response for a third set of interior models (C1-C4 in Tab. 2) selected from an ensemble of models generated by a simultaneous optimization (Militzer et al. 2020) an interior structure and wind profile using a Monte Carlo approach. These models relate wind velocity-depth profiles to contributions in  $J_n$  using the thermal wind equation (TWE) as presented in Kaspi et al. (2018). Whereas Kaspi et al. (2018) used a single reference interior density structure found an optimized wind profile to match the odd zonal harmonics ( $J_3, J_5, \dots$ ), models C1-C4 attempt to match the even  $J_n$  with a combined contribution from the CMS interior structure and a wind profile using the TWE, while also attempting to match the odd  $J_n$  with the same wind profile. The parameterization of the interior structure in these models is similar to Wahl et al. (2017b). In practice these models are found able to match the *Juno*  $J_n$ , while better fulfilling the composition constraints from *Galileo*, due to the added freedom for the wind profile to account for a portion of the even  $J_n$ . These models result in larger  $\Delta J_n$  than Kaspi et al. (2018), particularly for  $J_6$ , and consequently lead to a slightly larger range in calculated  $k_{nm}$ .

### 3. RESULTS

#### 3.1. Convergence behavior

Here we study the convergence behavior of the CMS calculations for the equilibrium tidal response. This is of particular relevance when considering the higher degree Love numbers, as the tesseral moments of various degree,  $n$ , and order,  $m$ , can exhibit very different convergence behavior. This must be accounted for when reporting the numerical precision of a given  $k_{nm}$  calculated using the

CMS approach.

First, we study the discretization error by comparing the calculated  $k_{nm}$  for models for an increasing number of spheroids,  $N_l$  in the CMS calculation. Fig. 4 shows the convergence of the calculated  $k_{22}$  and  $k_{20}$  from 64 layers to the 512 layer model used in the rest of of the paper, and then up to 2048 layers. The difference between 512 and 1024 layers in the upper panel shows that 512 layers is sufficient to derive  $k_{22}$  to 6 significant digits. Meanwhile,  $k_{20}$  is only converged to the level of  $\sim 10^{-4}$ .  $k_{22}$  has a notably better convergence behavior than the higher degree Love numbers, which converge to  $\sim 10^{-5}$  when  $n = m$ , but with precision worsening as  $n - m$  increases. Up to degree  $n = 5$ , all  $k_{nm}$  are converged with  $N_l$  to better than  $2 \times 10^{-4}$ . In the current implementation, calculations more than 1000 layers are too computationally expensive for a detailed study, although the accelerated approach for the 2D CMS approach (Militzer et al. 2019) could be adapted to the 3D CMS method.

Next, we study the convergence behavior of the various  $k_{nm}$  from a single model through the iterative procedure. Whereas the Love numbers with order  $m \neq 1$  are converged to at least the level of the discretization error after 25 iterations, those with  $m = 1$  require  $\sim 150$  iterations. This can be attributed to the fact that the rearranging of the spheroid centers of mass described in Sec. 2.2 is slower than the convergence of the shape of the spheroid. In the original implementation of the CMS tidal response (Wahl et al. 2016, 2017a), the convergence of  $k_{31}$  and  $k_{51}$  were essentially halted at a precision of  $\sim 10^{-2}$ – $\sim 10^{-3}$ . This appears to have a negligible effect on the results for the other  $k_{nm}$  where  $n \neq 1$ . The convergence behavior over the course of the calculation is also found to be nearly independent of the strength of the tidal perturber  $q_{\text{tid}}$ .

Finally, we look at the convergence behavior of  $k_{nm}$  with tidal perturber strength,  $q_{\text{tid}}$ . Fig. 5 shows three examples for the convergence of a given  $k_{nm}$ , where the satellite’s orbital distance is fixed, while  $q_{\text{tid}}$ , or equivalently the satellite mass, is varied. Starting from a magnitude of  $q_{\text{tid}}$  much greater than the corresponding satellite value, the value of  $k_{nm}$  initially approaches a constant value

with decreasing  $|q_{\text{tid}}|$ . This constant demonstrates the expected tidal response in the limit of small perturbation. However, at the smallest values of  $|q_{\text{tid}}|$ , the value of  $k_{nm}$  diverges again from the constant value, due to the limited numerical precision of the calculation. In the case of Io's  $k_{22}$ , the CMS calculation can clearly resolve a small non-linearity at the corresponding  $q_{\text{tid}}$ .

However, the convergence behavior for other  $k_{nm}$  with  $q_{\text{tid}}$  differ significantly from  $k_{22}$ . From the very same CMS calculation at Io's orbital distance, the value of  $k_{20}$  at the satellite  $q_{\text{tid}}$  is affected by this limited precision. In this case we cannot resolve any non-linearity in  $k_{20}$ , and we instead report the linear-regime value, evaluated at the  $q_{\text{tid}} \sim -10^{-5}$ , where the change in  $k_{20}$  between different  $q_{\text{tid}}$  is at a minimum. In Fig. 5 the reported  $k_{nm}$  is shown in green. The precision of this  $k_{nm}$  is limited by the fact that it is derived by taking the finite difference of Eq. 5 between two calculations performed with different  $q_{\text{tid}}$ . This uncertainty in the calculated linear regime  $k_{nm}$  limits the precision of  $k_{20}$  and the other  $k_{n0}$ , and is included into the reported numerical uncertainty.

The precision of the higher degree  $k_{nm}$  becomes increasingly limited as the satellite becomes more distant due to the decrease in  $q_{\text{tid}}$ . For example, the reported  $k_{33}$  for Callisto is the linear-regime result, whereas the larger  $q_{\text{tid}}$  of Io or Europa allows  $k_{33}$  to be calculated directly. These limits to precision of the linear regime  $k_{nm}$  calculation, are well below the potential sensitivity of *Juno*. The sensitivity of *Juno* is discussed in detail in Sections 3.3 and 3.4, but can be estimated taking a relatively optimistic assumption that *Juno* can detect a signal with a maximum strength of  $\sim 1$   $\mu\text{gal}$ . If the signal from  $C_{20}$  considered in Fig.5 were modified to account for a 1  $\mu\text{gal}$  change in the maximum anomaly, it would cause a corresponding  $\sim 0.01$  change in  $k_{20}$ , which is two orders of magnitude larger than the estimated numerical uncertainty. However, directly using the value calculated at the satellite  $q_{\text{tid}}$  can result in a significant miss-reporting of some  $k_{nm}$ , when the magnitude of  $q_{\text{tid}}$  is sufficiently small.

### 3.2. Tidal response from Galilean satellites

Tab. 3 tabulates the calculated Love numbers for the equilibrium tidal response of Jupiter to Io. Independent calculations with the identical, reference interior model (A1) were performed at the satellites perijove and apojove, yielding a linear correction with orbital distance,  $dk_{nm}/dR_{\text{sat}}$  in units of Jupiter’s equatorial radius.

The Love numbers for a non-rotating analogue planet are also tabulated. As was noted in previous work with the CMS method,  $k_{nm}$  for a non-rotating planet are independent of  $m$ , while for the rapidly rotating Jupiter these values diverge as a result of rotational flattening. The value of  $k_{22} = 0.5897$  for the reference Jupiter model with rotation is significantly higher than the non-rotating case with  $k_{22} = k_{20} = 0.5364$ .

A similar disparity is seen when the CMS result is compared to the Radau-Darwin approximation, commonly used for tides on bodies with less significant rotational flattening. The normalized moment of inertia ( $C/Ma^2$ ) can be calculated directly from the CMS interior density structure (Hubbard & Militzer 2016). The calculated moment of inertia  $C/Ma^2 = 0.2639$ , would correspond to a  $k_{22} \sim 0.524$  under this approximation.

As described in Section 3.1, the table notes whether the CMS calculation is able to resolve non-linear behavior with  $q_{\text{tid}}$ . The numerical uncertainty represents the estimated discretization error for the reported 512 layer CMS calculation. In the cases where the non-linear behavior cannot be resolved at Io’s  $q_{\text{tid}}$ , we report the linear regime result and include the corresponding uncertainty in the reported numerical uncertainty. At the strength of Io’s perturbation all values of  $k_{nm}$  with  $m \neq 0$  can resolve non-linearity up to degree  $n = 10$ , while non-linearity is not resolved for any  $k_{nm}$  with  $m = 0$ .

For Io specifically, we also considered the full suite of interior models (A1-C4) tuned to fit the

observed low order zonal harmonics  $J_2$ ,  $J_4$  and  $J_6$ , as described in Sec. 2.3. These are tabulated as “*err interior*”, and in most cases represent a range less than one order of magnitude larger than the numerical precision. Likewise, the range for each Love number from the two sets of interior models constructed with consideration of the deep winds (Sec. 2.4) are tabulated as “*err winds K18*” and “*err winds M19*”. Even with their density contributions completely omitted, the range of  $k_{nm}$  predicted for wind profiles differ from the reference model (A1) by an amount smaller than could be observed by *Juno*. The error reported in “*k<sub>nm</sub> perijove*”, includes the maximum deviations from the different interior and wind profiles, along with the estimated numerical error and error propagated from uncertainties in physical constants. The For  $k_{22}$ , the largest source of uncertainty comes not from interior structure or winds, but from propagating the  $\sim 4$  km uncertainty on Jupiter’s observed radius into  $q_{\text{rot}}$ , and thus to the rotational flattening of the body. In spite of our conservative estimates of the various sources of uncertainty, the combined uncertainty remains well below the expected sensitivity of *Juno*. For instance, an optimistic sensitivity of a  $\sim 1 \mu\text{gal}$ , suggests an uncertainty two orders of magnitude larger than greatest disparity in  $k_{22}$  between models with different interior structures or winds. This suggests that the  $k_{nm}$  are extremely well determined by the low-order gravitational harmonics, and thus provide little additional information to constrain the deep interior structure of the planet.

Tab. 3 also presents the value of  $k_{nm}$  for the reference interior model at apojove, along with the corresponding derivative with orbital distance,  $dk_{nm}/dR_{\text{sat}}$ . For  $n < 4$  the variation in  $k_{nm}$  from orbital distance is small compared to the numerical uncertainty and ranges from different interior models. However, in the case of  $k_{42}$  the deviation of  $k_{nm}$  between apojove and perijove is much more substantial. The same is true for other higher degree  $k_{nm}$  where  $m \neq n$ , although in most cases this effect is likely below detectability. The one possible exception is for  $k_{20}$ , where, despite  $dk_{nm}/dR_{\text{sat}}$  being smaller than the reported uncertainties, independent calculations yield a signal with consistent

amplitude, in which the observable  $J_2$  varies by a magnitude similar to *Juno*'s uncertainty (Iess et al. 2018).

For the reference interior model (A1), identical calculations were performed for the three other Galilean satellites, and tabulated in Tabs. 4–6 and for the Sun in 7. These tables have been truncated to discount  $k_{nm}$  that would produce signals well below the detectability of *Juno*; the full tables (up to  $n = 16$ ) can be found in the supporting data. For these bodies, the reported uncertainty is the numerical uncertainty plus the uncertainty on  $q_{\text{rot}}$ , as reported for Io, but without the additional ranges from different interior density profiles or winds.

The qualitative behavior of  $k_{nm}$  is similar between satellites, although the precise values differ due to non-linearity in the response to both  $q_{\text{tid}}$  and  $R/r_J$ . As described in Wahl et al. (2016), the rotational flattening of Jupiter leads to a splitting of the  $k_{nm}$  values from those calculated for a non-rotating analogue planets. Most of the low-degree  $k_{nm}$  agree with those presented in Nettelmann (2019). Our calculated value for Io's  $k_{22}$  matches theirs to within our reported uncertainty. The largest disparities occur for  $k_{nm}$  with  $m = 1$ , with their values for Io's  $k_{31}$  and  $k_{51}$  differing from those presented here by  $\sim 30\%$  and  $\sim 15\%$  respectively. This disparity can likely be attributed to the treatment of the average force and spheroid centers of mass described in Sec. 2.2, as they used the older CMS implementation that suffered from the offset center of mass. The match between the independent calculations also becomes poorer for  $k_{nm}$  with higher degree  $n$  and for more distant satellites, which may reflect limitations of numerical precision with small  $|q_{\text{tid}}|$  summarized in Sec. 3.1. Nonetheless, the good agreement supports our conclusion of the insensitivity of the equilibrium tidal response to the details of the interior model, including those based on a different equation of state.

The magnitude of the splitting becomes more significant with increasing degree  $n$  and orbital distance. It is also noteworthy that higher degree  $k_{nm}$  with  $m \neq n$  show a much greater difference

from the non-rotating analogue, than the  $k_{nm}$  with  $m = n$ . This can be related to the geometry of the tesseral harmonics in Fig. 2, as harmonics with  $m \neq n$  are those that exhibit nodes in longitude and therefore map differently onto a flattened spheroid, than those without such nodes.

Fig. 6 shows an example of how two such  $k_{nm}$  vary with orbital distance. For  $k_{22}$  the change is relatively modest, with the value predicted for Europa differing by only  $\sim 3 \times 10^{-4}$ , likely too small of a difference to be observable to Juno, but still an order of magnitude larger than the uncertainty introduced from considering different interior models that fit the observed  $J2$ - $J6$ . In contrast,  $k_{42}$  at Callisto's orbital distance is over 18 times larger than for Io. As a result, the satellite dependent equilibrium tidal response is most readily observable for  $k_{42}$ , even though the magnitude of the signal corresponding to  $k_{22}$  and  $k_{33}$  are larger. In the case of the tide raised by the Sun, Tab. 7, the splitting of the calculated higher-degree  $k_{nm}$  become quite extreme, but the corresponding harmonic  $C_{nm}$  strength decays rapidly with degree  $n$ , such that all  $C_{nm}$  with  $n > 2$  are far below levels detectable by *Juno*. The lack of a substantial satellite dependence for  $k_{22}$  does not rule out the possibility of a satellite dependent dynamic contribution (Notaro et al. 2019). In fact, given the small difference in equilibrium  $k_{22}$  calculated for the various satellites, measurement of disparate  $k_{22}$  at the different satellite orbital frequencies might be taken as evidence for a dynamic tidal contribution.

In order to model the complete equilibrium tidal bulge on Jupiter, the contributions from all four of the satellites must be taken into account. Since for each satellite  $q_{\text{tid}} \ll q_{\text{rot}}$ , it is a reasonable assumption to treat the full tesseral harmonic as a linear superposition of contributions from the separate satellites. Rearranging Eqs. 3 and 5, the contribution of a satellite to the tesseral harmonics is given by

$$C_{nm} = C_{nm,0} \cos(m(\Phi - \Phi_0)) \quad (15)$$

$$S_{nm} = C_{nm,0} \sin(m(\Phi - \Phi_0)), \quad (16)$$

where  $\Phi$  and  $\Phi_0$  are the phase of the satellite and a reference phase, and

$$C_{nm,0} = 2 \frac{(n-m)!}{(n+m)!} \left(\frac{m_s}{M}\right) \left(\frac{r_{\text{eq}}}{R}\right)^{n+1} P_n^m(0) k_{nm}, \quad (17)$$

with  $k_{nm}$  at a given orbital separation  $R$  given by the various tables.  $R$  varies over the course of an elliptical orbit, leading to small changes in both  $r_{\text{eq}}/R$  and  $q_{\text{tid}}$ .

Since the three satellites with the strongest tidal perturbations are in a 4:2:1 orbit resonance, the time-dependent, equilibrium tidal bulge is dominated by a signal that repeats once every orbit of Ganymede. It is convenient for visualization to set the reference phase  $\Phi_0$  in Eq. 15 to that of Io's orbit. In this frame of reference the primary contribution to the tidal bulge from Io remains fixed, contributing only to  $C_{nm}$ , while contributions from the other satellites cause temporal variations in  $C_{nm}$  and  $S_{nm}$  from that baseline value. Fig. 7 shows this repeating pattern in the tidal response in terms of  $C_{22}$  and  $S_{22}$ , over a single orbit of Ganymede with  $t = 0$  taken to be at inferior conjunction of Io and Ganymede. Fig. 8 shows the corresponding pattern for  $C_{nm}$  of other selected low-degree harmonics.

Due to the coincidental match of *Juno*'s orbital period with this resonance, the spacecraft perijoves occur within a limited range of  $\Phi_{\text{Io}} - \Phi_{\text{Europa}}$ . The point in the orbital cycle for each *Juno* perijove are shown on the  $C_{nm}$  curves in Figs. 7 and 8, for both the completed (PJ1-PJ21) and currently projected (PJ22-PJ35) perijoves. If the *Juno* spacecraft orbit is altered during the extended mission to allow for a larger range of  $\Delta\Phi$ , then the sensitivity of the *Juno* gravity solution to the satellite specific  $k_{nm}$  would increase.

While  $k_{20}$  is not directly observable through the means that  $k_{nm}$  with  $m > 0$  are, the top panel of Fig. 8 suggests an indirect means of measuring it. The equilibrium  $C_{20}$  is varies with Io's orbital distance. The total equilibrium tidal contribution to  $J_2$  is  $\sim 6.6 \times 10^{-8}$  and would be embedded in much larger contributions from the interior or winds. However the variations from Io's orbital



eccentricity would cause the total  $J_2$  to vary by  $\sim 1.5 \times 10^{-9}$ . This is roughly an order of magnitude smaller than the reported  $J_2$  uncertainty of the [Iess et al. \(2018\)](#) gravity solution, but may become detectable as the uncertainty decreases over the course of the mission.

### 3.3. Gravity anomaly from the Love numbers

A straightforward way of estimating the relative detectability of a given  $k_{nm}$  is to calculate the maximum gravitational anomaly associated with that specific Love number. Starting with the corresponding tesseral gravity harmonic  $C_{nm}$  from Eqn. 17, the gravity anomaly at the sub-satellite point ( $\mu = 0, \phi = 0$ ) that results from adding that tesseral signal to an axisymmetric gravity solution is

$$\delta g_r = C_{nm} \frac{P_n^m(0)}{n+1} \frac{GM_J}{r_J^2}. \quad (18)$$

Fig. 9 shows the relative magnitude of the anomaly for various  $k_{nm}$  calculated for each of the four satellites at their perijove. Io's  $k_{22}$  yields a  $\delta g_r \sim 0.085$  mgal, while Europa and Ganymede's  $k_{22}$  have a corresponding  $\delta g_r$  roughly one order of magnitude smaller, and Callisto an order of magnitude smaller yet. In the lower panel of Fig. 9, we see that the most readily detectable higher order Love numbers,  $k_{33}$ ,  $k_{42}$  and  $k_{31}$ , have  $\delta g_r$  values on the order of a  $\mu$ gal.

We can attempt to predict which Love numbers *Juno* is sensitive to by comparing the calculated gravity anomaly magnitude with an estimate for observational uncertainty. For instance, Fig. 3 of [Iess et al. \(2018\)](#) presents the residual gravitational accelerations for a single close approach of the spacecraft, during which the minimum uncertainty is on the order of  $\sim 0.1$  mgal. Using this value in conjunction with Fig. 9, we would thus predict *Juno* to be sensitive to only  $k_{22}$  and  $k_{20}$  for Io, and not to any  $k_{nm}$  from the other satellites. In the following section we consider instead the sensitivity to a time-integrated signal from the calculated equilibrium tides.

### 3.4. Sensitivity of *Juno* Doppler measurements to the calculated Love numbers

The *Juno* Gravity Science experiment uses measurements of the Doppler shift of the radio signal transmitted by the spacecraft to determine the time history of the spacecraft velocity projected onto the direction to the Earth tracking station,  $\dot{\rho}$ . The velocity component is measured with accuracy of about  $\sigma_{\dot{\rho}} = 5\mu\text{ms}^{-1}$  for averaging times of one minute, limited primarily by fluctuations in the water content in the Earth's troposphere (Asmar et al. 2017). The velocity measurements are used to estimate corrections to models of the forces acting on the spacecraft, including Jupiter's equilibrium gravity field and its tidal perturbations characterized by the Love numbers. In order to estimate Love numbers  $k_{nm}$  from the Doppler measurements, we calculate the partial derivative for the change in velocity per unit change in the value of the Love number,  $\partial\dot{\rho}/\partial k_{nm}$  for each measurement time. Given a calculated value of  $k_{nm}$ , the magnitude of the predicted velocity change due to each Love number is

$$\dot{\rho}_{pred} = k_{nm} \frac{\partial\dot{\rho}}{\partial k_{nm}}. \quad (19)$$

The top panel of Fig. 10 shows the predicted Doppler velocity,  $\dot{\rho}_{pred}$ , as a function of time for the thirteenth closest approach of the *Juno* spacecraft to Jupiter (labeled PJ13), on 24 May 2018, due to the tides raised on Jupiter by the four Galilean satellites, each characterized by the calculated values of the Love number  $k_{42}$ . The signals are well above the measurement noise level,  $\sigma_{\dot{\rho}}$ , for about one hour centered on closest approach and, as expected, Io raises the strongest tidal effect on Jupiter. Equivalent signatures from  $k_{22}$  are nearly 200 times larger than those from  $k_{42}$ , therefore we choose not to display both effects, as they are difficult to display using the same scale for the signal strength. Eventually the values of the Love numbers will be adjusted to best fit the measurements from several *Juno* perijoves. While the data are still being calibrated, we use the theoretical values of the Love numbers, while estimating the larger equilibrium gravitational signature to reduce the chance of mismodeling of the tide signatures corrupting the equilibrium gravity field estimate.

The middle panel of Fig. 10 shows the degree-4 tidal signal from Io during PJ13, for different values of the order  $m$ . Likewise, the signal of these parameters are well above the noise cut-off level, hence we expect them to affect the reduction of the *Juno* Doppler data and require them to be properly modeled. Furthermore, the predicted Doppler signal from tides is a function not only of the Love number and tide raising body, but also of the *Juno*-Io phase angle (bottom panel).

In order to compare the size of the effects of the different Love numbers, Fig. 11 shows the signal-to-noise ratio ( $SNR$ ) during *Juno* thirteenth perijove (PJ13) for Love numbers  $k_{nm}$ . The  $SNR$  is defined here as the ratio of the nominal value of the Love number and the uncertainty in its estimated value,  $\sigma_{k_{nm}}$ , from the Doppler data when only the Love number is estimated. The uncertainty is given by

$$\sigma_{k_{nm}} = \frac{\sigma_{\dot{\rho}}}{\sqrt{\sum(\partial\dot{\rho}/\partial k_{nm})}}, \quad (20)$$

where the summation is over all Doppler measurements for a single perijove. The  $SNR$  is then given by

$$SNR_{nm} = \frac{k_{nm}}{\sigma_{k_{nm}}}. \quad (21)$$

This definition of the  $SNR$  allows a comparison of the amplitude of the effect of the different equilibrium Love numbers on the Doppler measurements. Fig. 11 shows that the  $SNR$  for Love numbers of degree and order 3 through degree and order 5 ranges from 2 to 2400, hence most of them are, in principle, detectable in the *Juno* data. In general, the Love numbers cannot be independently estimated because their signatures in the Doppler data are not orthogonal to the other Love numbers, and are not orthogonal to the equilibrium gravity signature or several other parameters describing other force models. Therefore, *Juno* is likely to be able to accurately estimate values and uncertainties for Love number with  $SNR$  greater than  $\sim 100$ , but inclusion of nominal values for lower  $SNR$  Love numbers is important to avoid aliasing of small tidal signals into other gravity parameters.

Using this conservative threshold for  $SNR$ , Fig. 11 suggests that *Juno* will be able to estimate Io's

$k_{33}$ ,  $k_{31}$ , and  $k_{42}$ , with  $k_{44}$  lying near the threshold. Likewise, it suggests that *Juno* may be able to estimate  $k_{22}$  for the other three Galilean satellites. The solar tide is below the threshold with its  $k_{22}$  having a  $SNR \sim 30$ , and the next most significant tidal perturber, Jupiter’s satellite Amalthea, yields an  $SNR$  an order of magnitude smaller than the Sun. If the signals could be sufficiently separated down to an  $SNR \sim 10$ , then degree 3 and 4 Love numbers might be detected for Europa and Ganymede, along with  $k_{53}$  for Io. The conclusions of  $SNR$  analysis are, therefore, more optimistic towards the number of detectable  $k_{nm}$  than would be predicted from the gravity anomaly magnitudes alone (Sec. 3.3). Comparing these predictions to the lower panel of Fig. 9, suggests that *Juno* is sensitive to tides with a maximum gravity anomaly as low as  $\sim 1\mu gal$ .

#### 4. CONCLUSIONS

In this work, we calculate the equilibrium tidal response of Jupiter to its four Galilean moons and the Sun. We present these as a series of tables that report the  $k_{nm}$  for each body, characterizing their dependence on orbital distance, and the estimated uncertainty from the numerical method, physical parameters, interior density structure and winds. We find an equilibrium  $k_{22} = 0.58976 \pm 0.0001$  for Io, consistent with previous calculations (Wahl et al. 2016; Nettelmann 2019), that is remarkably insensitive to details of the interior structure model, once fitted to the low degree axisymmetric gravity solution ( $J_2$ ,  $J_4$ , and  $J_6$ ) from *Juno* (Iess et al. 2018). This means that measurement of  $k_{22}$  by *Juno* will not yield additional constraints on the interior structure via the equilibrium tidal response. However, this insensitivity to interior models also means that *Juno* has the opportunity to unambiguously detect dynamic contributions to the tidal response. Should dynamic contributions be detected, they may yield independent information regarding interior structure or processes, although a comprehensive theoretical predictions for such a dynamic response have not been performed.

We introduce improvements to the CMS method for tidal response calculations, which eliminate

the previously described center of mass shift resulting from the original implementation. The improvement allows us to correctly resolve the Love numbers of order  $m = 1$  (i.e.  $k_{31}$  and  $k_{51}$ ). We find that for the tides experienced by Jupiter, that the predictions of the other  $k_{nm}$  using the previous method (Wahl et al. 2016, 2017a; Nettelmann 2019) are consistent, at least within the expected sensitivity of *Juno*. It remains to be shown whether the improved method has a more profound affect on predictions for close-in extrasolar planets, where the tidal perturbations can be several orders of magnitude stronger.

In Sec. 3.4 we studied the sensitivity of the *Juno* Doppler measurements to the calculated equilibrium tidal response. By finding the signal to noise ratio for the calculated  $k_{nm}$ , we show that *Juno* is sensitive to both the high-degree ( $n > 2$ ) Love numbers of Io, as well the  $k_{2m}$  of Europa, Ganymede, Callisto and the Sun. This is important for two reasons: First, it motivates the need for inclusion of the higher order tidal components in the analysis and interpretation of *Juno* Doppler data. The signals from these higher order tides are sufficiently large, that mischaracterizing them could lead to their misinterpretation as contributions from from another source (i.e. interior density structure or deep winds). Second, they suggest that multiple  $k_{nm}$  may be detectable by *Juno*. In principle, this could provide a test of the theoretical predictions for the rotationally induced splitting and orbital dependence of the equilibrium  $k_{nm}$  (Wahl et al. 2017a). They may also offer independent measurements from  $k_{22}$  to detect or characterize a dynamic contribution to the tides.

## ACKNOWLEDGMENTS

The work of Sean Wahl and Burkhard Militzer was carried out at the University of California, Berkeley, with the support of the National Aeronautics and Space Administration, Juno Program. The work of Marzia Parisi and William M Folkner was carried out at the Jet Propulsion Laboratory, California Institute of Technology, under a contract with the National Aeronautics and Space

Administration. Government sponsorship acknowledged.

## REFERENCES

- Asmar, S. W., Bolton, S. J., Buccino, D. R., et al. 2017, *Space Science Reviews*, 213, 205
- Becker, A., Lorenzen, W., Fortney, J. J., et al. 2015, *Astrophysical Journal, Supplement Series*, 215, doi:10.1088/0067-0049/215/2/21
- Campbell, J., & Synnott, S. 1985, *Astron. J.*, 90, 364
- Cao, H., & Stevenson, D. J. 2017, *J. Geophys. Res. Planets*, 122, 686
- Chabrier, G., Mazevet, S., & Soubiran, F. 2019, *The Astrophysical Journal*, 872, 51
- Chaplin, W. J., & Miglio, A. 2013, *Annual Review of Astronomy and Astrophysics*, 51, 353
- Debras, F., & Chabrier, G. 2019, *The Astrophysical Journal*, 872, 100
- Durante, D., Guillot, T., & Iess, L. 2017, *Icarus*, 282, 174
- Folkner, W. M., Iess, L., Anderson, J. D., et al. 2017, *Geophys. Res. Lett.*, 44, 4694
- Fuller, J. 2014a, *Icarus*, 242, 283
- Fuller, J. W. 2014b, PhD thesis
- Gavrilov, S. V., & Zharkov, V. N. 1977, *Icarus*, 32, 443
- Guillot, T., Miguel, Y., Militzer, B., et al. 2018, *Nature*, 555, doi:10.1038/nature25775
- Hubbard, W. B. 2012, *Astrophys. J.*, 756, L15
- . 2013, *Astrophys. J.*, 768, 43
- Hubbard, W. B., & Militzer, B. 2016, arXiv:1602.05143
- Iess, L., Folkner, W., Durante, D., et al. 2018, *Nature*, 555, doi:10.1038/nature25776
- Jacobson, R. A. 2003
- . 2013
- Kaspi, Y. 2013, *Geophys. Res. Lett.*, 40, 676
- Kaspi, Y., Guillot, T., Galanti, E., et al. 2017a, *Geophys. Res. Lett.*, 44, 5960
- . 2017b, *Geophys. Res. Lett.*, doi:10.1002/2017GL073629
- Kaspi, Y., Galanti, E., Hubbard, W., et al. 2018, *Nature*, 555, doi:10.1038/nature25793
- Lainey, V., Jacobson, R. A., Tajeddine, R., et al. 2017, *Icarus*, 281, 286
- Marley, M. S., & Porco, C. C. 1993, *Icarus*, 106, 508
- Miguel, Y., Guillot, T., & Fayon, L. 2016, *Astron. Astrophys.*, 114, 1
- Militzer, B. 2009, *Phys. Rev. B*, 79, 155105
- . 2013, *Phys. Rev. B*, 87, 014202
- Militzer, B., & Hubbard, W. B. 2013, *Astrophys. J.*, 774, 148
- Militzer, B., Hubbard, W. B., Vorberger, J., Tamblyn, I., & Bonev, S. A. 2008, *The Astrophysical Journal*, 688, L45
- Militzer, B., Soubiran, F., Wahl, S., & Hubbard, W. 2016, *Journal of Geophysical Research E: Planets*, 121, doi:10.1002/2016JE005080
- Militzer, B., Wahl, S., & Hubbard, W. B. 2019, *The Astrophysical Journal*, 879, 78
- . 2020, in preparation
- Morales, M. A., McMahon, J. M., Pierleone, C., & Ceperley, D. M. 2013, *Phys. Rev. Lett.*, 110, 065702
- Murray, C., & Dermott, S. 1999, *Solar System Dynamics* (Cambridge University Press)
- Nettelmann, N. 2017, *Astronomy & Astrophysics*, 606, A139
- . 2019, *The Astrophysical Journal*, 874, 156
- Nettelmann, N., Becker, A., Holst, B., & Redmer, R. 2012, *Astrophys. J.*, 750, 52
- Nettelmann, N., Holst, B., Kietzmann, A., et al. 2008, *Astrophys. J.*, 683, 1217
- Notaro, V., Durante, D., & Iess, L. 2019, *Planetary and Space Science*, 175, 34
- Perdew, J. P., Burke, K., & Ernzerhof, M. 1996, *Phys. Rev. Lett.*, 77, 3865
- Saumon, D., & Guillot, T. 2004, *Astrophys. J.*, 609, 1170
- Schöttler, M., & Redmer, R. 2018, *Journal of Plasma Physics*, 84, 755840401
- Seiff, A., Kirk, D. B., Knight, T. C. D., et al. 1998, *J. Geophys. Res.*, 103, 22857
- Stevenson, D. J., & Salpeter, E. E. 1977, *Astrophys J Suppl.*, 35, 239
- von Zahn, U., Hunten, D. M., & Lehmacher, G. 1998, *J. Geophys. Res.*, 103, 22815
- Vorberger, J., Tamblyn, I., Militzer, B., & Bonev, S. 2007, *Phys. Rev. B*, 75, 024206
- Wahl, S., Hubbard, W., & Militzer, B. 2016, *Astrophysical Journal*, 831, doi:10.3847/0004-637X/831/1/14
- Wahl, S. M., Hubbard, W. B., & Militzer, B. 2017a, *Icarus*, 282, 183
- Wahl, S. M., Hubbard, W. B., Militzer, B., et al. 2017b, *Geophys. Res. Lett.*, 44, 4649
- Wisdom, J., & Hubbard, W. B. 2016, *Icarus*, 267, 315
- Zharkov, V. N., & Trubitsyn, V. P. 1978, *Physics of Planetary Interiors* (Pachart), 388

**Table 1.** Jupiter Tidal Parameters

Body	Parameter		Parameter
Jupiter	$GM$	126686534.911 km <sup>3</sup> /s <sup>2</sup>	$q_{\text{rot}}$ 0.089195 ± 1.5 × 10 <sup>-5</sup>
	$r_{\text{eq}}$	71492. ± 4. km	
	$T_{\text{rot}}$	0:9:55:29.711 D:H:m:s	
Io	$GM$	5962.0 km <sup>3</sup> /s <sup>2</sup>	$R_{\text{pj}}$ 5.87534 r <sub>J</sub>
	$a$	421769. km	$R_{\text{aj}}$ 5.92372 r <sub>J</sub>
	$e$	0.0041	$q_{\text{tid,pj}}$ -6.87587 × 10 <sup>-7</sup>
			$q_{\text{tid,aj}}$ -6.79199 × 10 <sup>-7</sup>
Europa	$GM$	3201.6 km <sup>3</sup> /s <sup>2</sup>	$R_{\text{pj}}$ 9.29196 r <sub>J</sub>
	$a$	671079. km	$R_{\text{aj}}$ 9.48158 r <sub>J</sub>
	$e$	0.0101	$q_{\text{tid,pj}}$ -9.44995 × 10 <sup>-8</sup>
			$q_{\text{tid,aj}}$ -9.11439 × 10 <sup>-8</sup>
Ganymede	$GM$	9891.0 km <sup>3</sup> /s <sup>2</sup>	$R_{\text{pj}}$ 14.95833 r <sub>J</sub>
	$a$	1070042.8 km	$R_{\text{aj}}$ 14.97629 r <sub>J</sub>
	$e$	0.0006	$q_{\text{tid,pj}}$ -6.99812 × 10 <sup>-8</sup>
			$q_{\text{tid,aj}}$ -6.97297 × 10 <sup>-8</sup>
Callisto	$GM$	7181.3 km <sup>3</sup> /s <sup>2</sup>	$R_{\text{pj}}$ 26.15424 r <sub>J</sub>
	$a$	1883000. km	$R_{\text{aj}}$ 26.52298 r <sub>J</sub>
	$e$	0.007	$q_{\text{tid,pj}}$ -9.50535 × 10 <sup>-9</sup>
			$q_{\text{tid,aj}}$ -9.11439 × 10 <sup>-9</sup>
Sun	$GM$	132712440041.93938 km <sup>3</sup> /s <sup>2</sup>	$R_{\text{pj}}$ 10357.8 r <sub>J</sub>
	$a$	778.57 × 10 <sup>6</sup> km	$R_{\text{aj}}$ 11422.8 r <sub>J</sub>
	$e$	0.0489	$q_{\text{tid,pj}}$ -2.82816 × 10 <sup>-9</sup>
			$q_{\text{tid,aj}}$ -2.10853 × 10 <sup>-9</sup>

<sup>a</sup>Physical parameters in left column from <https://ssd.jpl.nasa.gov/horizons.cgi>. Derived tidal parameters at perijove and apjove in right column.

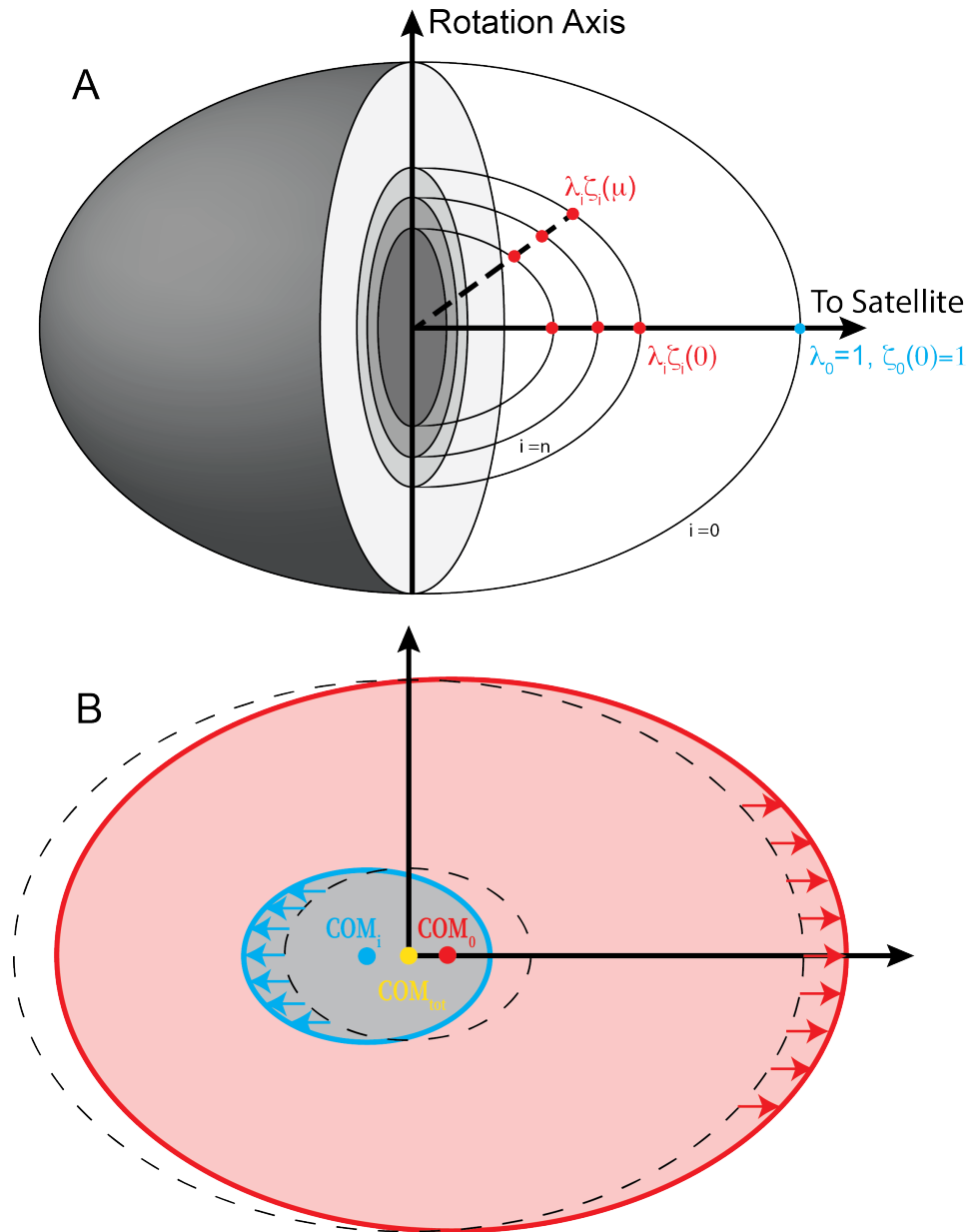


**Figure 1.** Conceptual diagram of a Concentric Maclaurin Spheroid (CMS) model with a tidal perturbation from a satellite. A: The density structure is discretized into a superposition of constant density spheroids. The surface of spheroid  $i$  is described by the fraction  $\zeta_i$  of the equatorial radius  $\lambda_i$ , at coordinates  $\mu, \phi$ . B: In the presence of a tidal perturber the spheroids surfaces and centers of mass (COM) are permitted to respond to the external potential under the constraint of constant volume, such that the outermost spheroids shift towards the satellite while the innermost spheroids shift away from the satellite. The total center of mass remains fixed at the origin.



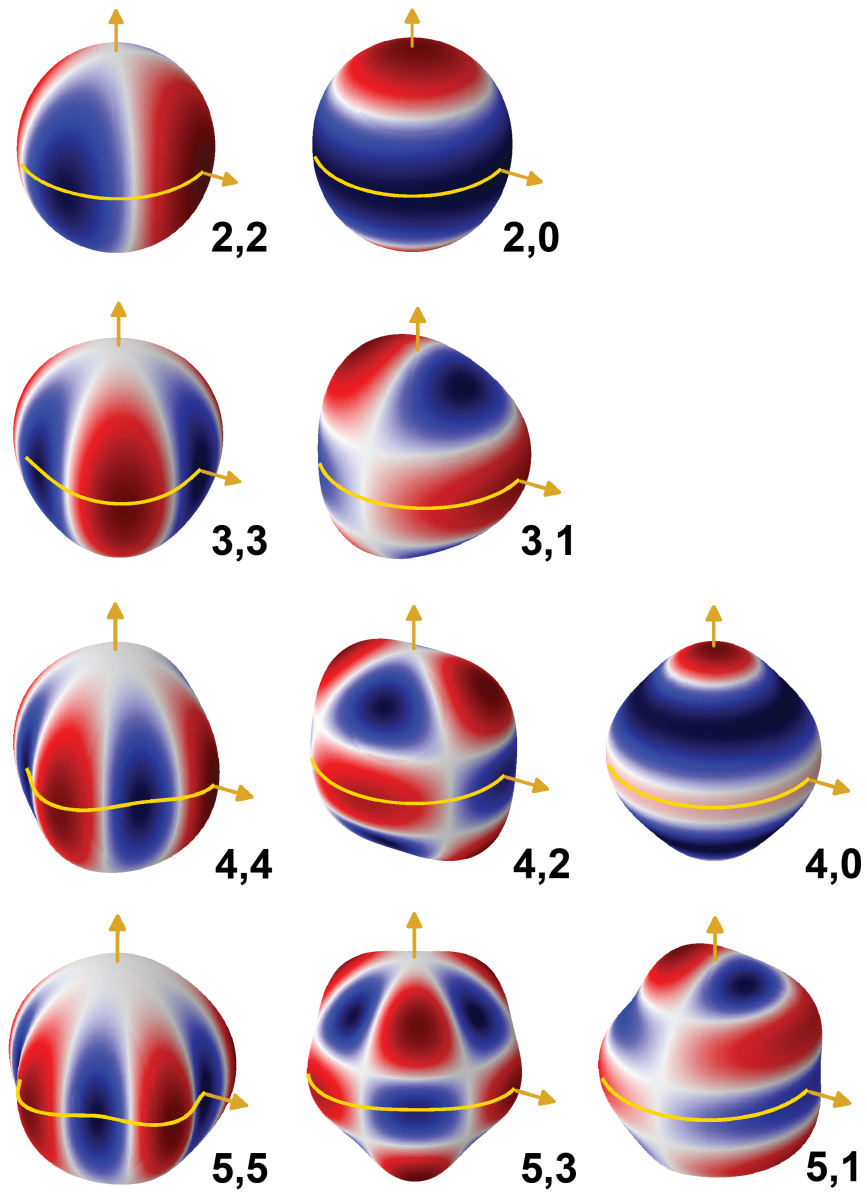


**Figure 2.** Shapes of the gravity harmonics,  $C_{nm}$ , labeled by degree  $n$  and order  $m$ , where  $|m| \leq n$ . Yellow arrows show the pole and indicate the direction of the tidal perturber, and yellow line shows the equator.

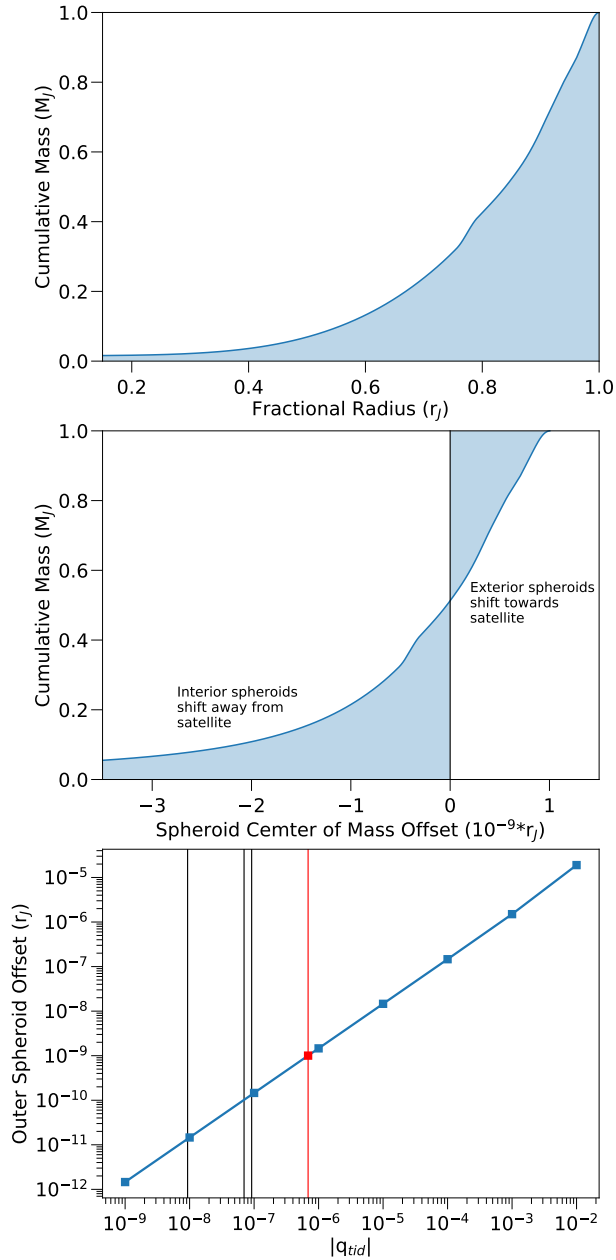


**Figure 3.** Top panel: Cumulative mass  $m/M_J$  as a function of fractional radius  $\lambda$  for a representative interior model. Middle Panel: The offset of spheroid center of mass as a function of cumulative mass for CMS models with tidal response to Io. Spheroids exterior to  $m/M_J \sim 0.5$  have center of mass (COM) shifts towards the satellite, while interior spheroids have COM shifts away from the satellite. The total center of mass of the planet is constrained to lie at the origin. Bottom panel: The magnitude of the COM shift for the outermost layer ( $\lambda = 0$ ) as a function of tidal perturber strength,  $q_{tid}$ . Vertical lines denote  $q_{tid}$  of the four Galilean moons, with Io shown in red.

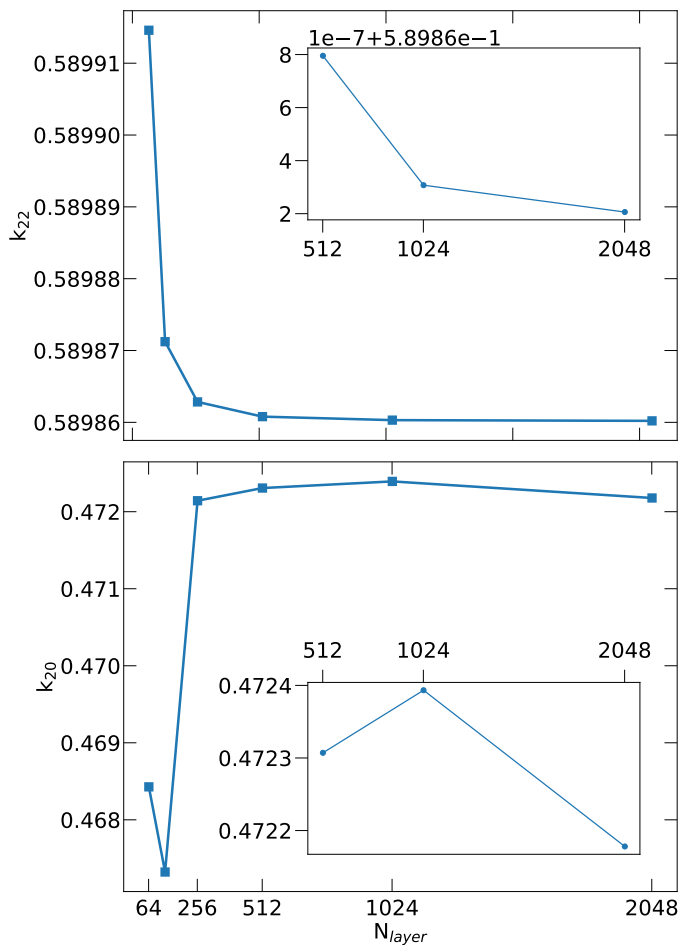


**Figure 4.** Convergence of Love numbers  $k_{22}$  and  $k_{20}$  with the number of spheroids,  $N_L$ , in the CMS model. The numerical precision for Love numbers of different degree and order are limited by their convergence at  $N_L = 512$ . The Love numbers of order  $m = 0$  are determined to significantly lower precision than the other Love numbers.

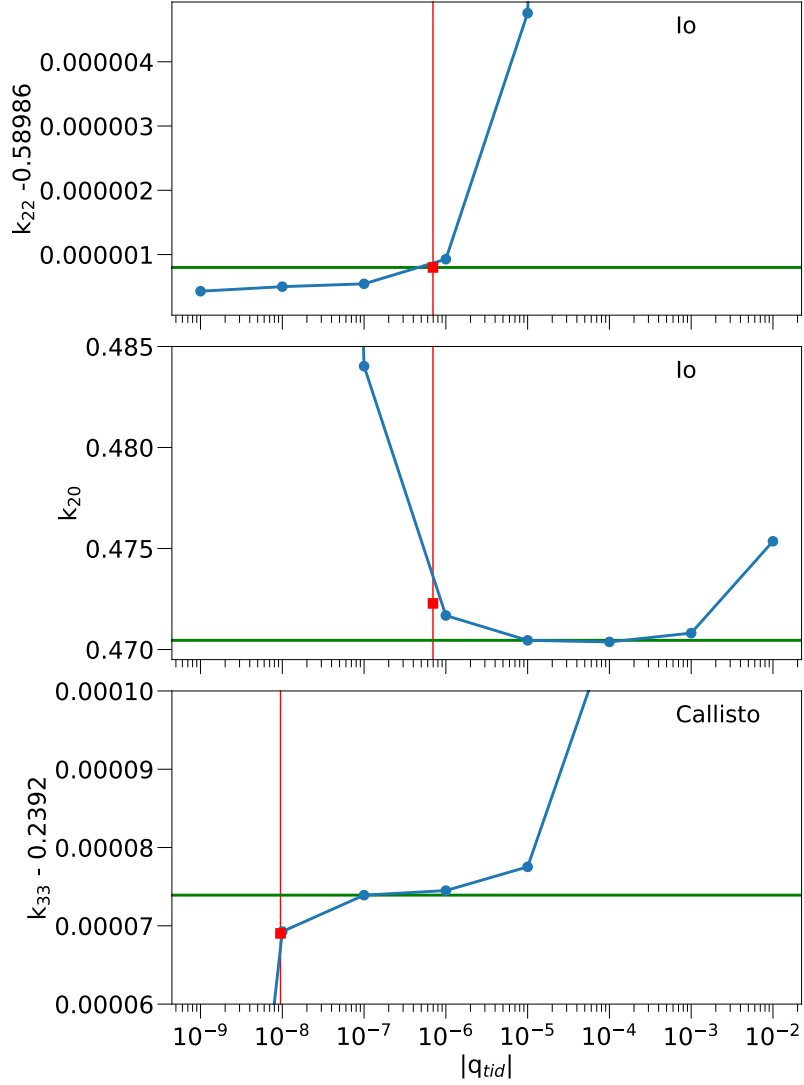


**Figure 5.** Representative examples of the convergence of various Love numbers as a function of tidal perturber strength,  $q_{tid}$  (blue). The red vertical line denotes the value of  $q_{tid}$  corresponding to the perturbing satellite. Shown in red is the value obtained directly from the CMS simulation with  $|q_{tid}|$  corresponding to the satellite. Shown in green is the reported value for  $k_{nm}$ , which depends on whether the CMS simulation at the correct  $q_{tid}$  resolves a value better than the estimate for the linear regime. (Top)  $k_{22}$  for a satellite at Io’s orbital distance, which resolves the non-linearity of the Love number. (Middle)  $k_{20}$  for a satellite at Io’s orbital distance. In this case the best estimate of the linear regime occurs at  $q_{tid,io}$ . This is the case for all Love numbers of order 0 regardless of satellite. (Bottom) For Callisto, the smaller magnitude of  $q_{tid}$  means the best estimate of  $k_{33}$  is the estimate of the linear regime, even though  $k_{33}$  value is resolved directly for Io.

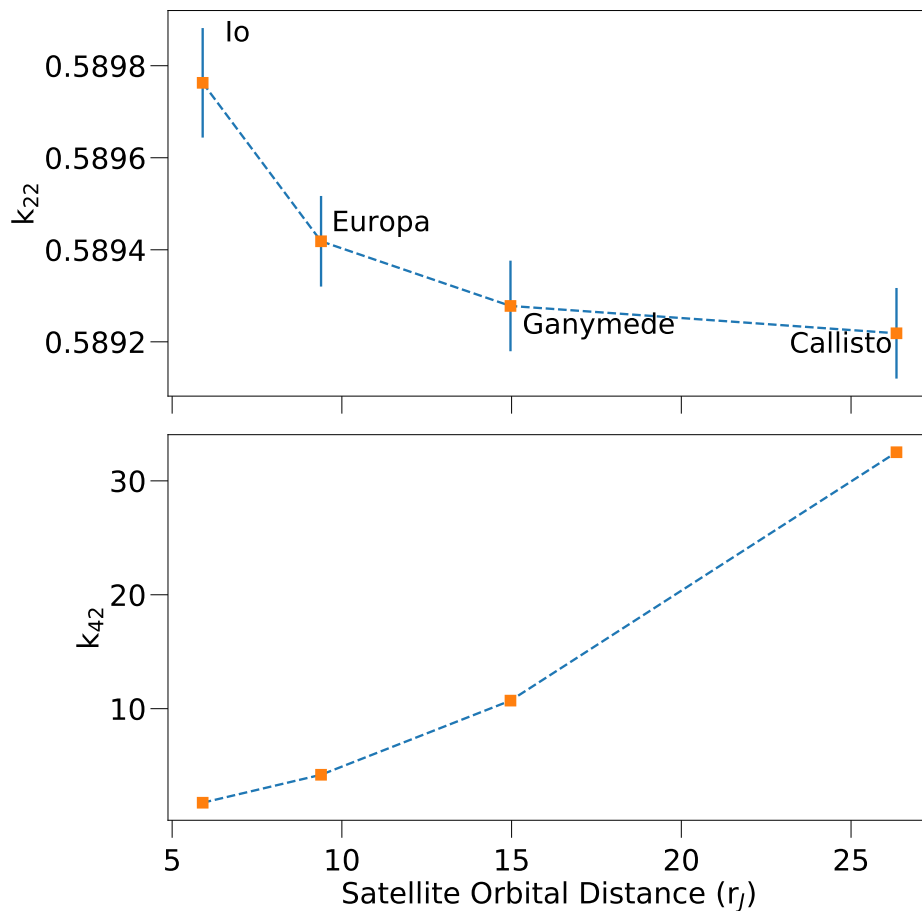


**Figure 6.** The dependence of Love numbers  $k_{22}$  and  $k_{20}$  on the orbital distance of the four Galilean moons. The relative strength of the effect becomes more significant for both larger degree  $n$ , and for larger  $n - m$ . The effect is relatively small for  $k_{22}$  (top panel) and more significant for  $k_{42}$  (bottom panel). For Io, the errorbars show the range of  $k_{nm}$  for interior models matching the observed  $J_n$ .

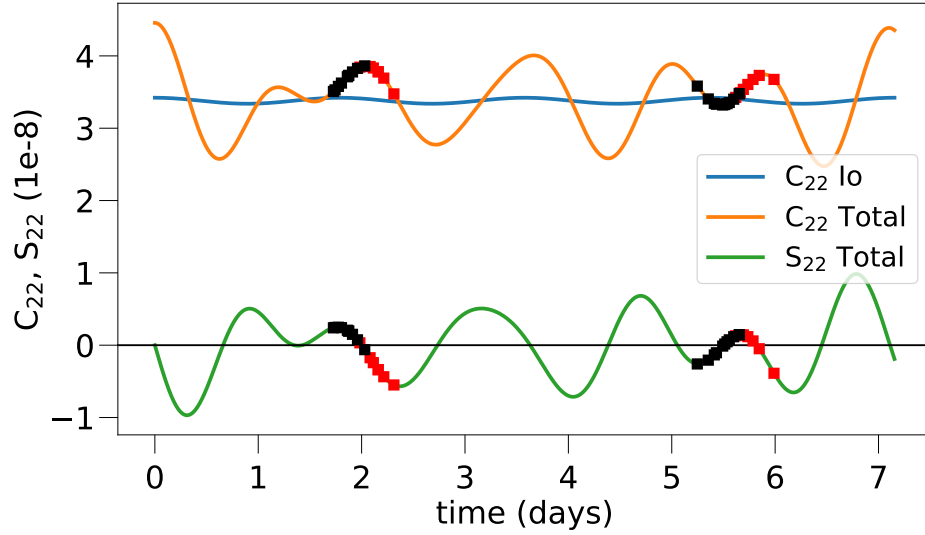


**Figure 7.** Combined contribution to the tesseral gravity harmonics  $C_{22}$  (yellow) and  $S_{22}$  (green) from all Galilean moons over the course of one orbit of Ganymede (4 orbits of Io), with  $t = 0$  at the inferior conjunction of Io and Ganymede. The coordinates are chosen such that Io contributes only to  $C_{nm}$ , with  $S_{nm}$  contributions arising from the other satellites. The contribution from  $C_{nm}$  from Io alone is shown in blue. The squares show the point in the cycle at *Juno* perijove, with completed PJ1-PJ21 in black and projected PJ22-PJ35 in red.

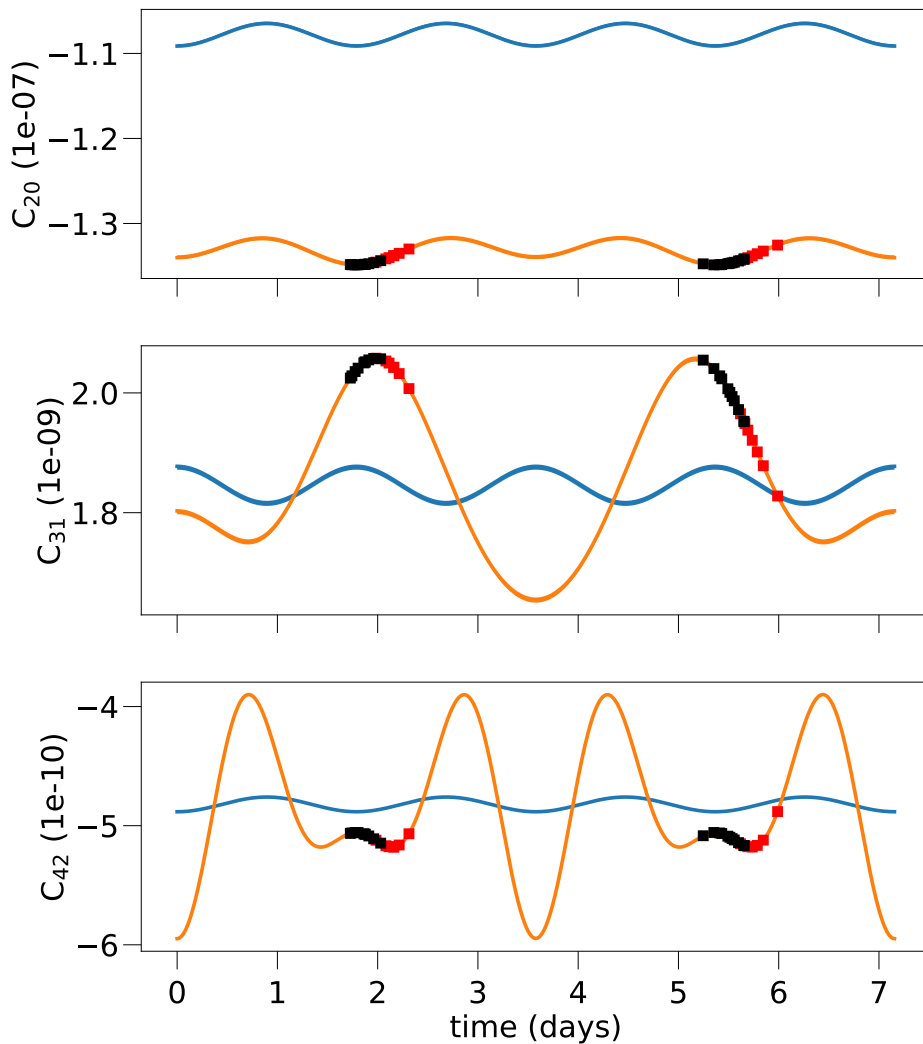


**Figure 8.** Combined contribution to  $C_{nm}$ , (yellow) from all Galilean moons over the course of one orbit of Ganymede, as in Fig. 7. The contribution from  $C_{nm}$  from Io is shown in blue. The squares show the point in the cycle at *Juno* perijove, with completed PJ1-PJ21 in black and projected PJ22-PJ35 in red.

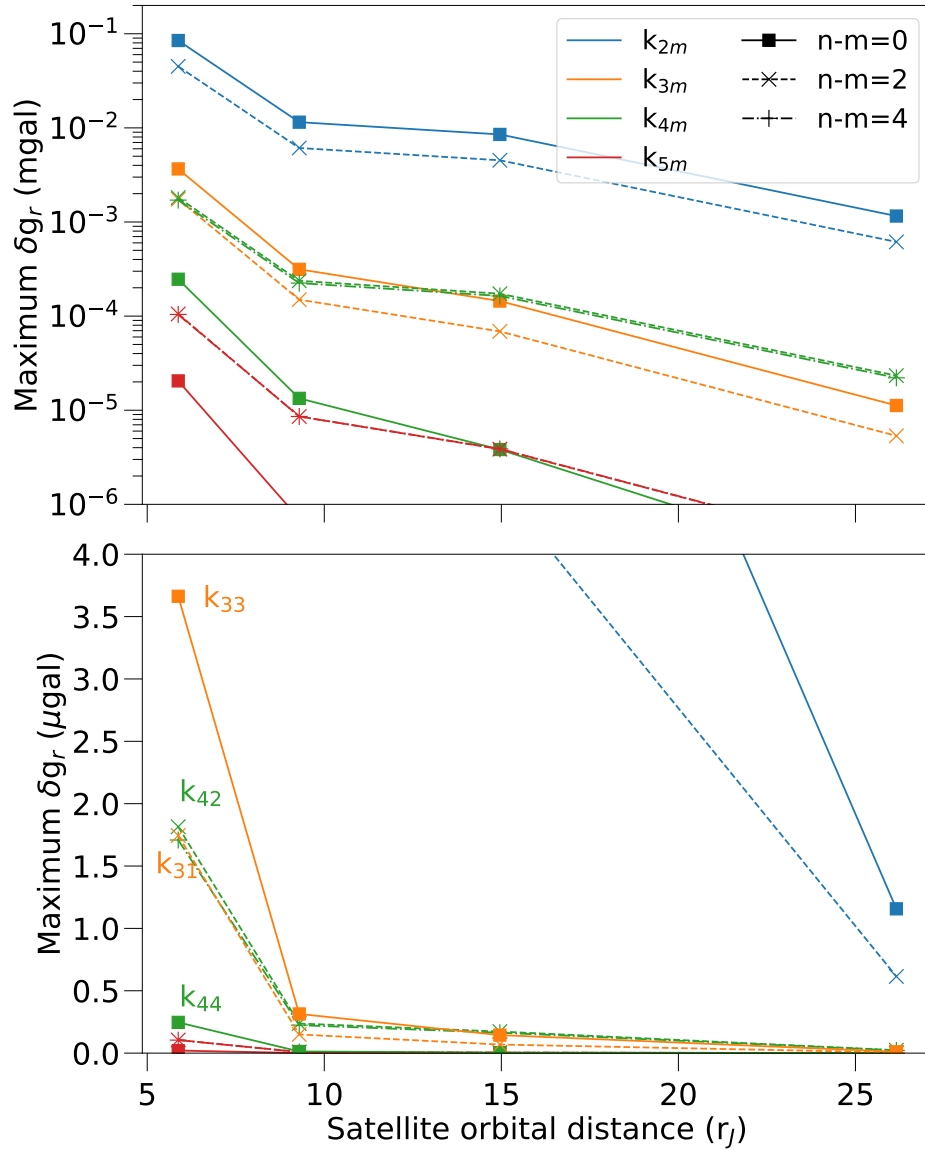


**Figure 9.** Top panel: maximum gravity anomaly,  $\delta g_r$ , at the surface resulting from the calculated  $k_{nm}$  for each Galilean satellites. Bottom panel: same but on a linear scale at the  $\mu\text{gal}$  level. The most readily observable  $k_{nm}$  with  $n > 2$  are labeled.



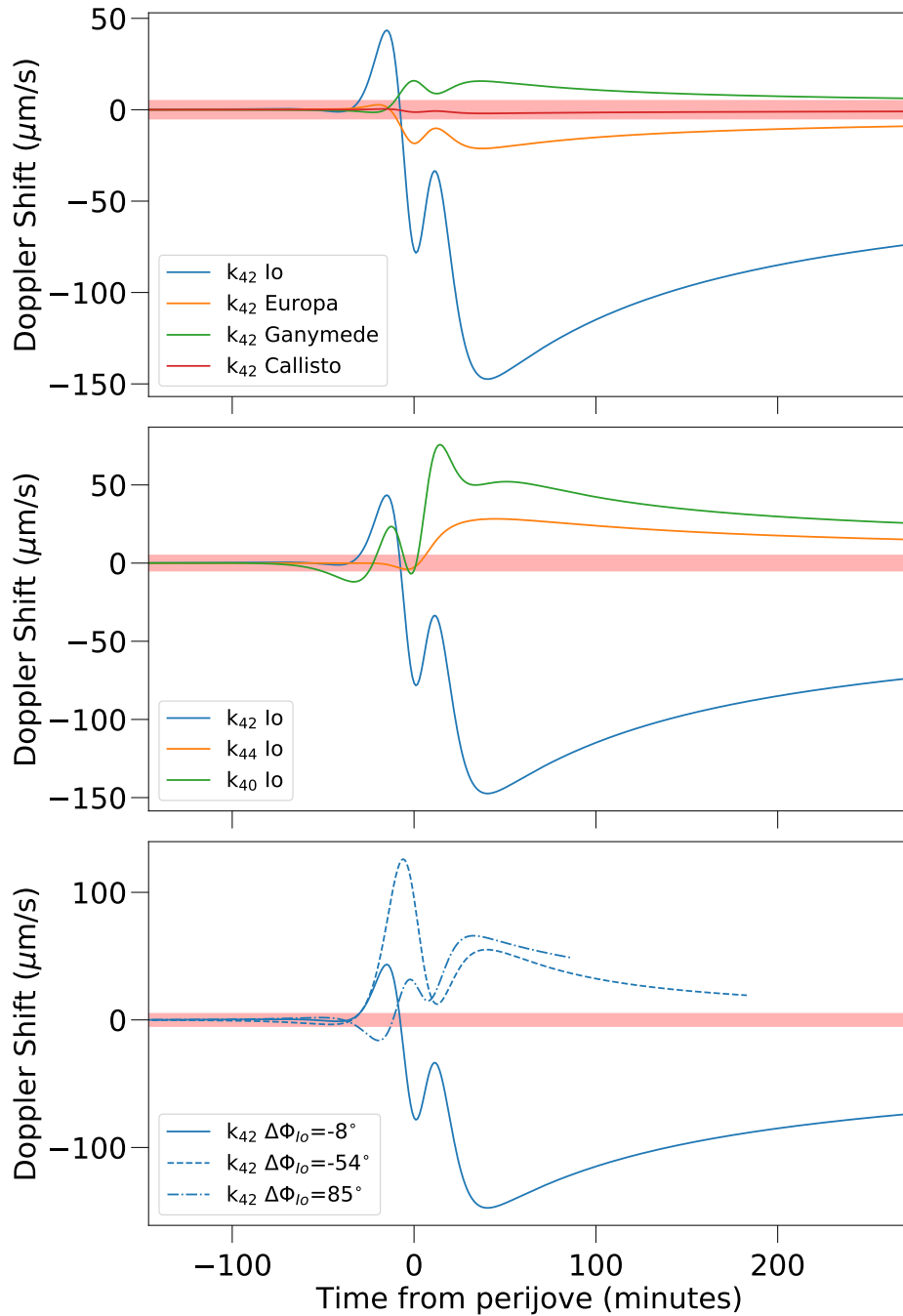


**Figure 10.** Top panel: Doppler shift as a function of time near *Juno* perijove resulting from adding an equilibrium  $k_{42}$  with the magnitude for each Galilean satellite from this paper at their PJ13 positions. The red filled region shows the noise level for data about the optimized gravity solution for this perijove. Middle panel: Same as top panel but showing the  $k_{44}$ ,  $k_{42}$  and  $k_{40}$  for Io. Bottom Panel: same as top panel, but comparing  $k_{42}$  from Io for PJ13, PJ06 and PJ03, during which the difference in longitude between *Juno* and Io ( $\Delta\Phi_{\text{Io}}$ ) is  $-8^\circ$ ,  $-54^\circ$ , and  $85^\circ$ , respectively.

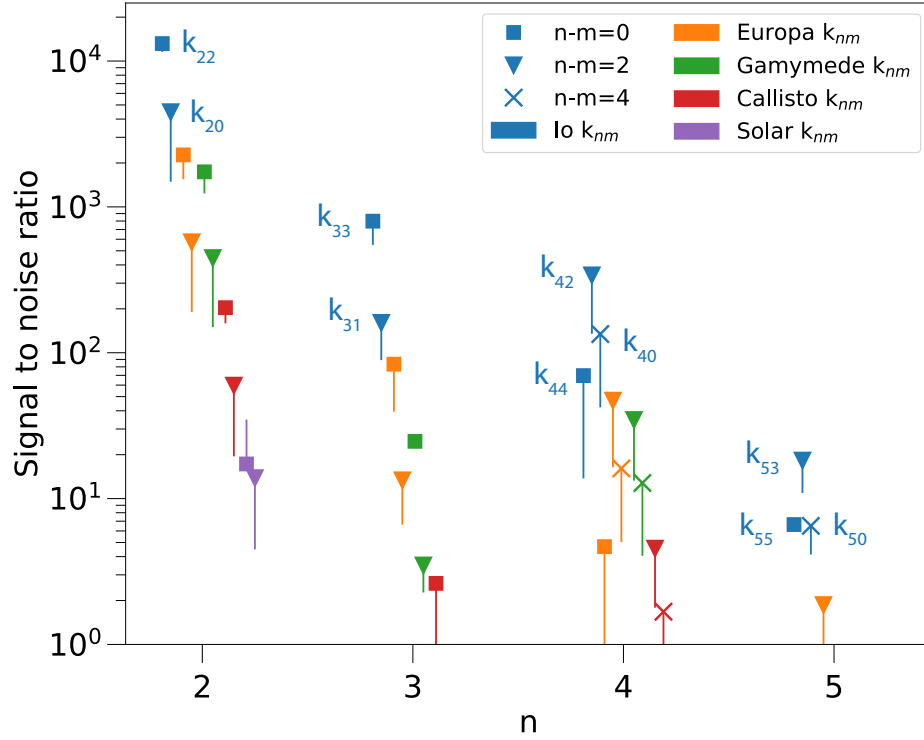


**Figure 11.** Signal to noise ratio for time-integrated Doppler shift profiles (Fig. 10) resulting from adding the calculated equilibrium  $k_{nm}$  for each Galilean satellite and the Sun from this paper at their PJ13 positions. During PJ13 *Juno* was close to the Io sub-satellite point ( $\Delta\Phi_{\text{Io}} = -8^\circ$ ). The error bars show the range of *SNR* including two other close approaches PJ06 and PJ03, with  $\Delta\Phi_{\text{Io}} = -54^\circ$  and  $85^\circ$ , respectively.

**Table 2.** Interior Models

Model <sup>a</sup>	Description	$J_2$	$J_4$	$J_6$	$J_8$	$J_{10}$
Target $J_n$	PJ06 gravity solution <sup>b</sup>	<b>14696.51</b>	<b>-586.60</b>	<b>34.20</b>	-2.42	0.17
A1	helium rain onset pressure	14696.51	-586.613	34.202	-2.458	0.202
A2	helium rain layer $\Delta S$	14696.51	-586.609	34.202	-2.458	0.202
A3	dilute core $Z$ , $r = 0.7$	14696.51	-586.602	34.204	-2.457	0.202
A4	dilute core $Z$ , $r = 0.5$	14696.51	-586.603	34.203	-2.457	0.202
B1	<a href="#">Kaspi et al. (2018)</a> longitude independent	14696.01	-586.561	34.200	-2.459	0.202
B2	<a href="#">Kaspi et al. (2018)</a> longitude dependent	14697.04	-586.463	34.200	-2.460	0.202
C1	<a href="#">Militzer et al. (2020)</a> model 1	14694.90	-586.524	34.502	-2.504	0.207
C2	<a href="#">Militzer et al. (2020)</a> model 2	14695.27	-586.721	34.511	-2.505	0.207
C3	<a href="#">Militzer et al. (2020)</a> model 3	14694.92	-586.562	34.499	-2.504	0.207
C4	<a href="#">Militzer et al. (2020)</a> model 4	14695.08	-586.566	34.503	-2.504	0.207

<sup>a</sup> All A and B models fit  $J_2$  and  $J_4$  by tuning  $S$  and  $Z_2$ . Description for A models specifies parameter tuned to fit  $J_6$ . B models are fit to the  $\Delta J_n$  from [Kaspi et al. \(2018\)](#) optimized wind profiles. C models are more complicated interior profiles from [Militzer et al. \(2020\)](#), where the  $\Delta J_n$  correspond to a wind profile optimized simultaneously with interior density profile. Model A1 is used as the reference model in all tables and figures unless otherwise stated.

<sup>b</sup> Target  $J_n$  are from the PJ06 gravity solution [Iess et al. \(2018\)](#) with the calculated tidal contribution from Io removed.

Table 3. Calculated equilibrium Love numbers for Io

$n$	$m$	$k_{nm}$	nonrot	$k_{nm}$	perijove	$k_{nm}$	apojoove	$dk_{nm}/dR_{\text{sat}}$	non-linear	err numerical	err $q_{\text{rot}}$	err interior	err winds K18	err winds M20
2	2	0.536369		0.589759 <sup>+1.1e-04</sup> <sub>-1.3e-04</sub>		0.589749	-1.931e-04	True	±4.9e-07	±9.2e-05	+0.0e+00 -5.7e-06	+2.1e-05 -2.5e-05	+0.0e+00 -3.0e-05	
2	0			0.4699 <sup>+7.1e-04</sup> <sub>-7.8e-04</sub>		0.4699	-2.745e-04	False	±1.9e-04	±8.4e-05	+1.3e-04 -4.9e-04	+2.6e-05 -1.5e-05	+3.1e-04 -0.0e+00	
3	3	0.22434		0.23948 <sup>+6.8e-05</sup> <sub>-6.3e-04</sub>		0.23948	-9.256e-05	True	±1.5e-05	±5.3e-05	+0.0e+00 -1.9e-05	+0.0e+00 -8.8e-05	+0.0e+00 -5.5e-04	
3	1			0.19014 <sup>+5.7e-05</sup> <sub>-5.7e-04</sub>		0.19013	-1.556e-04	True	±1.1e-05	±4.5e-05	+0.0e+00 -1.4e-05	+0.0e+00 -7.0e-05	+0.0e+00 -5.0e-04	
4	4	0.12786		0.1353 <sup>+8.8e-04</sup> <sub>-8.9e-05</sub>		0.13529	-5.881e-05	True	±1.3e-05	±3.9e-05	+5.8e-05 -0.0e+00	+0.0e+00 -3.7e-05	+7.7e-04 -0.0e+00	
4	2			1.7432 <sup>+1.7e-03</sup> <sub>-8.5e-04</sub>		1.7702	5.589e-01	True	±1.1e-04	±2.9e-04	+6.2e-08 -6.8e-06	+0.0e+00 -4.4e-04	+1.3e-03 -0.0e+00	
4	0			1.8231 <sup>+2.3e-03</sup> <sub>-2.8e-03</sub>		1.8516	5.886e-01	False	±6.6e-04	±3.4e-04	+4.1e-04 -1.4e-03	+0.0e+00 -4.5e-04	+8.8e-04 -0.0e+00	
5	5	0.08354		0.08806 <sup>+1.2e-03</sup> <sub>-5.6e-05</sub>		0.08805	-4.136e-05	True	±1.1e-05	±3.1e-05	+9.1e-06 -8.1e-07	+0.0e+00 -1.3e-05	+1.2e-03 -0.0e+00	
5	3			0.81536 <sup>+6.7e-03</sup> <sub>-4.6e-04</sub>		0.82769	2.548e-01	True	±9.1e-05	±1.9e-04	+1.1e-04 -0.0e+00	+0.0e+00 -1.7e-04	+6.3e-03 -0.0e+00	
5	1			0.9406 <sup>+7.3e-03</sup> <sub>-5.4e-04</sub>		0.9551	2.998e-01	True	±1.0e-04	±2.4e-04	+1.9e-04 -0.0e+00	+0.0e+00 -2.1e-04	+6.7e-03 -0.0e+00	
6	6	0.059081		0.062151 <sup>+1.2e-03</sup> <sub>-1.0e-04</sub>		0.062149	-3.100e-05	True	±9.3e-06	±2.6e-05	+0.0e+00 -5.8e-05	+1.3e-05 -1.1e-05	+1.2e-03 -0.0e+00	
6	4			0.49903 <sup>+8.0e-03</sup> <sub>-5.2e-04</sub>		0.50647	1.538e-01	True	±7.0e-05	±1.5e-04	+0.0e+00 -2.1e-04	+2.4e-05 -8.7e-05	+7.8e-03 -0.0e+00	
6	2			5.8999 <sup>+6.1e-02</sup> <sub>-3.5e-03</sub>		6.0858	3.842e+00	True	±7.0e-04	±1.0e-03	+0.0e+00 -7.8e-04	+0.0e+00 -9.0e-04	+5.9e-02 -0.0e+00	
6	0			6.826 <sup>+1.1e-01</sup> <sub>-1.3e-02</sub>		7.043	4.498e+00	False	±5.6e-03	±1.6e-03	+7.3e-04 -4.7e-03	+0.0e+00 -1.1e-03	+1.0e-01 -0.0e+00	

<sup>a</sup>See supplementary material for full table in machine readable format, `io_2019_12_02.txt`.

<sup>b</sup>Total error of “ $k_{nm}$  perijove” includes uncertainties from columns 8-12.

**Table 4.** Calculated equilibrium Love numbers for Europa

$n$	$m$	$k_{nm}$ non-rotating	$k_{nm}$ perijove	$k_{nm}$ apojove	$dk_{nm}/dR_{sat}$	non-linear	err numerical	err $q_{rot}$
2	2	0.536369	$0.589414 \pm 9.2e-05$	0.589408	-4.782e-05	True	4.7e-07	9.1e-05
2	0		$0.469 \pm 1.3e-03$	0.469	-6.799e-05	False	1.2e-03	8.4e-05
3	3	0.22434	$0.23932 \pm 6.9e-05$	0.23931	-2.288e-05	True	1.5e-05	5.3e-05
3	1		$0.18986 \pm 5.7e-05$	0.18985	-3.849e-05	True	1.1e-05	4.5e-05
4	4	0.12786	$0.13519 \pm 5.3e-05$	0.13520	-1.450e-05	True	1.3e-05	3.9e-05
4	2		$4.1975 \pm 9.3e-04$	4.3662	8.893e-01	True	2.6e-04	6.7e-04
4	0		$4.407 \pm 9.1e-03$	4.584	9.367e-01	False	8.3e-03	8.0e-04
5	5	0.083531	$0.087982 \pm 3.9e-05$	0.087998	-8.086e-06	True	8.3e-06	3.1e-05
5	3		$1.9343 \pm 6.7e-04$	2.0114	4.056e-01	True	2.3e-04	4.4e-04
5	1		$2.2570 \pm 8.0e-04$	2.3477	4.771e-01	True	2.5e-04	5.5e-04

<sup>a</sup>See supplementary material for full table in machine readable format, `europa_2019_12_02.txt`.

**Table 5.** Calculated equilibrium Love numbers for Ganymede

$n$	$m$	$k_{nm}$ non-rotating	$k_{nm}$ perijove	$k_{nm}$ apojove	$dk_{nm}/dR_{sat}$	non-linear	err numerical	err $q_{rot}$
2	2	0.536369	$0.589274 \pm 9.2e-05$	0.589276	-1.177e-05	True	4.5e-07	9.1e-05
2	0		$0.4692 \pm 1.0e-03$	0.4692	-1.675e-05	False	9.6e-04	8.4e-05
3	3	0.22434	$0.23925 \pm 6.9e-05$	0.23925	-5.506e-06	False	1.6e-05	5.3e-05
3	1		$0.18975 \pm 5.8e-05$	0.18975	-9.348e-06	False	1.3e-05	4.5e-05
4	4	0.12786	$0.13515 \pm 5.3e-05$	0.13516	-2.322e-06	True	1.3e-05	3.9e-05
4	2		$10.7058 \pm 2.3e-03$	10.7315	1.418e+00	True	6.7e-04	1.7e-03
4	0		$11.26 \pm 1.7e-02$	11.29	1.494e+00	False	1.5e-02	2.0e-03
5	5	0.083498	$0.087961 \pm 3.3e-05$	0.087978	-4.765e-05	True	2.1e-06	3.1e-05
5	3		$4.9016 \pm 1.9e-03$	4.9138	6.467e-01	False	7.5e-04	1.1e-03
5	1		$5.7480 \pm 2.1e-03$	5.7622	7.608e-01	False	7.4e-04	1.4e-03

<sup>a</sup>See supplementary material for full table in machine readable format, `ganymede_2019_12_02.txt`.

**Table 6.** Calculated equilibrium Love numbers for Callisto

$n$	$m$	$k_{nm}$ non-rotating	$k_{nm}$ perijove	$k_{nm}$ apojove	$dk_{nm}/dR_{\text{sat}}$	non-linear	err numerical	err $q_{\text{rot}}$
2	2	0.536369	$0.589214 \pm 9.8\text{e-}05$	0.589218	-2.165e-06	False	5.0e-07	9.8e-05
2	0		$0.469 \pm 9.6\text{e-}03$	0.47	-3.073e-06	False	9.5e-03	1.0e-04
3	3	0.22434	$0.23922 \pm 4.8\text{e-}05$	0.23925	-1.060e-06	False	2.8e-05	2.0e-05
3	1		$0.18970 \pm 4.1\text{e-}05$	0.18972	-1.702e-06	False	2.1e-05	2.0e-05
4	4	0.12776	$0.13513 \pm 1.6\text{e-}05$	0.13518	-1.662e-06	True	1.1e-05	4.7e-06
4	2		$32.507 \pm 2.2\text{e-}03$	33.434	2.496e+00	True	2.0e-03	1.6e-04
4	0		$34.2 \pm 4.9\text{e-}01$	35.2	2.628e+00	False	4.9e-01	1.6e-03

<sup>a</sup>See supplementary material for full table in machine readable format, `callisto_2019_12_02.txt`.

**Table 7.** Calculated equilibrium Love numbers for Solar tide

$n$	$m$	$k_{nm}$ non-rotating	$k_{nm}$ perijove	$k_{nm}$ apojove	$dk_{nm}/dR_{\text{sat}}$	non-linear	err numerical	err $q_{\text{rot}}$
2	2	0.536369	$0.589186 \pm 9.1\text{e-}05$	0.589188	1.878e-12	False	4.6e-08	9.1e-05
2	0		$0.469 \pm 1.3\text{e-}03$	0.469	-3.756e-12	False	1.2e-03	8.4e-05

<sup>a</sup>See supplementary material for full table in machine readable format, `solar_2019_12_02.txt`.